2003

Automated simulation of 3-D crack propagation on bimaterial interfaces in semiconductor packages

Alexander F. (Frantz) Herr
Lehigh University

Recommended Citation

Herr, Alexander F. (Frantz), "Automated simulation of 3-D crack propagation on bimaterial interfaces in semiconductor packages" (2003). *Theses and Dissertations.* Paper 824.

Herr, Alexander F.

Automated Simulation of 3-D Crack Propagation on Bimaterial Interfaces...

January 2004

Automated Simulation of 3-D Crack Propagation on Bimaterial Interfaces in Semiconductor Packages

by

Alexander F. Herr

A Thesis
Presented to the Graduate and Research Committee
of Lehigh University
in Candidacy for the Degree of
Masters of Science

in
Mechanical Engineering and Mechanics

Lehigh University

December 2003

This thesis is accepted and approved in partial fulfillment of the requirements for the Master of Science.

12/4/03
Date

Thesis Advisor

Chairperson of Department

Acknowledgements

The author would sincerely like to thank the following groups and individuals for their contributions, without whom, this project would not have been possible:

- Dr. Nied for his guidance and encouragement
- Ümit Özkan for his many ideas, his time, his complete understanding of FRAC3D, his ability to modify FRAC3D in whatever means were necessary, and his over-riding optimism
- The SRC for funding the research
- My parents Dan and Caroline Herr and Amanda Ohs for their continual support and motivation

Table of Contents

Table of Figures

1.0 Abstract

Numerical simulation of the propagation of an arbitrarily shaped, three-dimensional crack can be a tedious, time-consuming process. This is especially true for 3-D cracks propagating on interfaces between various electronic materials in semiconductor packages. In addition to accurately accounting for the peculiar nature of the crack tip stress field associated with interface cracks, systematically "advancing" the crack must be based on an efficient numerical crack advance algorithm. Other important considerations for simulating 3-D crack propagation include: the creation of a solid model, the definition of the crack front, calculation of the stress intensity factors along the crack front, and finally, remeshing in the vicinity of the crack front after each incremental crack advance. In this study, a technique is described that combines the use of the ANSYS finite element software and a specialized finite element program, FRAC3D, developed at Lehigh University, to simulate crack front propagation of arbitrary 3-D cracks. This method uses the classical fatigue crack growth rate "law" developed by Paris and Erdogan to simulate stable crack growth under cyclic loading conditions. As a practical example in reliability analysis, the method is applied to a semiconductor package with a corner-crack. Results from two corner crack shapes, one fillet-shaped and one quarter-circular, are presented and compared. Plots for each are included showing the advancement of the crack front and the changes in the stress intensity factors, strain energy release rates, and phase angles over the twenty iterations performed.

2.0 Introduction

2.1 – Background Information

Components that contain bimaterial interfaces and that are subjected to residual or external stresses may experience failure within either of the constituent materials or along the interface. The failure mechanism depends on the geometry of the specimen, the loading, the matrix toughness, and the interface fracture resistance [1].

In layered structures such as electronic packages, the mechanical integrity is determined by the adhesive strength of the interfaces between dissimilar materials. The plastic flip-chip package is one such electronic package of particular interest. Since interfaces are numerous in a flip-chip package (i.e. die/passivation, passivation/underfill, underfill/solder mask, and solder mask/circuit board) and likely to debond, the interfacial strength at each interface plays a key role in determining the reliability of a flip-chip structure. These interfaces are common locations of failure initiation during testing, storage, and operation. Interfacial delamination between the epoxy underfill material and the silicon is the most often observed failure mode in these electronic packages. Therefore, accurate studies and simulations of interfacial adhesive strength and failure modes allow for improved understanding of the structural reliability [2].

By their nature, materials used in semiconductors packages have widely varying mechanical properties, including elastic modulus and coefficient of thermal expansion. The large differences in the material properties between silicon and epoxy underfill resins make interfacial boundaries the most common location for cracks to initiate and propagate [3]. A sketch with the locations of stress singularities annotated can be seen in

Figure 1. In the work described here, interface cracks originating and propagating out from the corner of a semiconductor chip package have been simulated using finite element software. Figure 2 is a schematic showing a corner crack that started on the bond plane of a bimaterial interface. The series of pictures in Figure 3 shows the progressive development of a corner crack. Values preceding TC are the number of thermal cycles undergone to produce the cracked image shown. Note the very low cycle fatigue and the severity of the damage done at these levels.

Simulating the progression shown in the C-SAM images of Figure 3 is the goal of this work; to produce a numerical simulation that imitates the movement of a crack front and gives a reasonable estimate of the number of thermal cycles to failure. Numerical simulations of fatigue failure can be performed in two types of analysis, two-dimensional and three-dimensional. Two-dimensional analyses are limited to applications in axi-symmetric, plane stress, and plane strain problems. Three-dimensional models are larger in terms of degrees of freedom and must represent a significant portion of the cracked body. In the tensile and thermal interface cracks presented here, three-dimensional models are required [4].

Creating a finite element model of a three-dimensional crack and simulating its propagation are tasks that many researchers are currently examining. The problem consists primarily of five steps, which generally are:

1) meshing the problem of interest
2) defining the crack
3) calculating stress intensity factors
4) driving the crack forward

5) moving the crack front nodes

The exact structure of the algorithm utilized here is detailed further in Section 5.0 The Propagation Algorithm. For crack propagation, repetition of steps two through five continues until an ending condition is satisfied, i.e. the crack reaches a specified length, a critical number of loading cycles have been completed, or the stress intensity factor exceeds the critical value, K_{IC}, and failure occurs or crack arrest occurs.

To simulate crack propagation, an equation must relate the stress intensity factor to the number of cyclic load applications and the crack length extension. This is done in the commonly used Paris-Erdogan crack growth law [5]

$$\frac{da}{dN} = C(\Delta K)^m, \qquad (1)$$

which represents the most basic form of this law for crack propagation in isotropic, homogeneous materials. Here ΔK is the stress intensity factor and C and m are material constants. Variables a and N are the length of the crack and the number of fatigue cycles applied to the crack, respectively. Solving for a or N can be accomplished by integrating Equation 1, where one of the values is generally selected in advance [5]. For example, a choice could be made to integrate for 300 cycles (N) to determine the crack extension (a) or for a crack extension of 0.1 millimeters (in a), to calculate the number of cycles (N).

$$\frac{da_i}{dN} = C_i(\Delta K_i)^{m_i} \qquad (2)$$

Equation 2 can be applied to 3-D numerical simulations using finite elements, where i is a single node from the set of crack front nodes. To propagate the crack, Equation 2 must be solved for each node along the crack front (see Figure 4). This equation allows the material properties C and m to vary by node; in homogeneous, isotropic materials these values remain constant for each crack front node. C and m are specific material properties that can be affected by environmental factors including corrosion and temperature and by material properties such as plastic zone size and microstructure. Specimen and crack geometry as well as loading configuration are taken into consideration during the calculation of the stress intensity factors.

$$N_f = \int_0^{N_f} dN = \int_{a_i}^{a_f} \frac{da_i}{C(\Delta K_i)^m} \tag{3}$$

In Equation 3, N_f is the final number of fatigue cycles for the crack to advance a given length, while a_i and a_f are the initial and final crack lengths, respectively. Usually, a_f is determined by the condition $K_I(a_f) = K_{IC}(a_f)$.

There are three distinct categories of basic fracture mechanisms. Mode I, denoted K_I, loading occurs for cracks under 'opening' or tensile loading, mode II, K_{II}, represents sliding or shearing, while mode III, K_{III}, is a tearing shear. A mixed mode problem is one in which combinations of the possible modes, explained above, exists. Equations 1-3 are generally only used in cases where the loading is purely mode I, mode II, or mode III. For these cases, ΔK can be computed and the appropriate form of the equation can be applied. Each stress intensity factor result for cracks in homogeneous materials is independent, but for interface problems, stress intensity factors for mode I and mode II are coupled and do not have the same physical meaning (or units) as in the homogeneous cases [3]. Thermal loading problems are a common example of a mixed mode problem with coupled stress intensity factors. To solve this type of problem, a new equation is introduced, similar to that found in [6].

$$\frac{da_i}{dN} = C_i\left(\Delta G_i\right)^{m_i} \tag{4}$$

C and m are material-related properties that must be determined empirically and ΔG is the strain energy release rate, which can be calculated based on the stress intensity factors [6]. In mixed-mode numerical simulations such as those performed here, the ΔG value calculated from the stress intensity factors, as shown in Equation 5, must be used, rather than the ΔK values. ΔG is used because it relates K_I, K_{II}, and K_{III} in their proper proportions. The interaction of the stress intensity factors and their relation to the strain energy release rate is of particular interest on bimaterial interfaces. In the following equations, subscripts 1 and 2 apply to the material properties of the attached materials. The following equation relates these parameters to the total strain energy release rate, G_{TOTAL},

$$G_{TOTAL} = \frac{1}{E_0 \cosh^2(\pi\varepsilon)}\left(K_I^2 + K_{II}^2\right) + \frac{(\mu_1 + \mu_2)}{4\mu_1\mu_2}K_{III}^2 . \tag{5}$$

where μ is the shear modulus and

$$\frac{1}{E_0} = \begin{cases} \dfrac{1}{2}\left(\dfrac{1}{E_1} + \dfrac{1}{E_2}\right) & \text{(plane stress)} \\ \dfrac{1}{2}\left(\dfrac{1-\nu_1^2}{E_1} + \dfrac{1-\nu_2^2}{E_2}\right) & \text{(plane strain)} \end{cases} \tag{6}$$

while ε is the oscillatory index defined as

$$\varepsilon = \frac{1}{2\pi}\ln\left[\frac{1-\beta}{1+\beta}\right]. \tag{7}$$

This equation introduces β, the second of Dundurs' parameters, which are quantifications of the elastic mismatch between the materials in bimaterial problems. Defined in terms of the material properties, Dundurs' parameters are [7]

$$\alpha = \frac{\mu_1(\kappa_2+1)-\mu_2(\kappa_1+1)}{\mu_2(\kappa_1+1)+\mu_1(\kappa_2+1)} \text{ and } \beta = \frac{\mu_1(\kappa_2-1)-\mu_2(\kappa_1-1)}{\mu_2(\kappa_1+1)+\mu_1(\kappa_2+1)}. \tag{8}$$

In the equations in 11, κ is used, and it is defined as

$$\kappa = \begin{cases} 3-4\nu & (\text{plane stress}) \\ \dfrac{3-\nu}{1+\nu} & (\text{plane strain}) \end{cases} \tag{9}$$

In bi-material interface fracture problems, typical stress intensity factor calculations yield meaningless results. An example of a problem that arises is that, without changing the dimensions of a problem, the sign of the stress intensity factor can change depending on the unit system (SI or English) chosen for the calculation. To obtain more conventional units, the stress intensity factors are "rotated" or normalized using the equations below, which can be derived from Rice [8] and which appear in their current form in Nied [3]

$$\hat{K}_I = K_I \cos(\varepsilon \ln L) - K_{II} \sin(\varepsilon \ln L) \tag{10}$$

$$\hat{K}_{II} = K_I \sin(\varepsilon \ln L) + K_{II} \cos(\varepsilon \ln L) \tag{11}$$

where ε is the oscillatory index and L is an arbitrary length. To adequately characterize the mode-mixity of a crack front, two phase angles are calculated to capture the ratio of shear to crack opening mode behavior. In contrast to two-dimensional crack problems where mode III is usually not considered, phase angles ψ and φ are required for three-dimensional cracks, as studied here. The phase angle ψ, is a measure of in-plane shear to normal stress, given by the ratio of K_{II} to K_I and is shown in Equation 12. The second phase angle, φ, is a ratio of tearing shear to normal stress, K_{III} to K_I and was suggested, as shown below in Equation 13, by Begley and Ambrico [4]

$$\psi = \tan^{-1}\left(\frac{K_{II}}{K_I}\right) \tag{12}$$

$$\varphi = \tan^{-1}\left(\frac{K_{III}}{K_I}\right). \tag{13}$$

Values for phase angle ranges from $\psi = 0^\circ$, pure tension (in the y-direction), to $\psi = \pm 90^\circ$, pure shear in the ± x directions while the second phase angle, φ, is similar with $\varphi = 0^\circ$ in tension and $\varphi = \pm 90^\circ$ as pure shear in the ± z direction.

A significant effect of the phase angles and the coupled mode I and mode II results is that to duplicate the conditions near a crack tip for a crack of length R, loaded in tension ($\psi = 0^\circ$), for another crack of length R' ($\neq R$), the body must be loaded by a combination of tension and shear [8]. In order to maintain consistency with the normalized K_{II} and K_I values, $\hat{K}_{II}$ to $\hat{K}_I$ respectively, phase angles must be "rotated" as well. The "rotated" phase angles are

$$\frac{\sigma_{xy}}{\sigma_{yy}} = \hat{\psi}_L = \tan^{-1}\frac{\hat{K}_{II}}{\hat{K}_I} = \psi + \varepsilon \ln L \tag{14}$$

and

$$\hat{\varphi}_L = \tan^{-1}\frac{K_{III}}{\hat{K}_I}. \tag{15}$$

In equations 14 and 15, L is an arbitrary length used for normalization. Although the unrotated phase angle, ψ, is strongly dependent on the unit system used, $\hat{\psi}_L$, is independent of unit system. For more information and a complete description of the derivation of equations 10, 11, and 14, see articles by Rice [8] and Nied [3], while equation 15 is attained in a similar fashion from an equation presented in [4].

2.2 – The State-of-the-Art

The methods for solving three-dimensional crack propagation and simulation are numerous and widely varying. Each researcher or group mentioned below approaches the problem using unique software or methods; there is no standard numerical approach to crack growth simulation and propagation. Since crack propagation is relevant to many catastrophic failures, research groups apply their solutions to relevant industrial problems, many of which are from the aeronautics industry where cyclic loading can cause catastrophic failures.

In [9], Lin and Smith began describing a technique they fully documented in [5, 10, and 11]. This scheme uses the ¼-point nodal displacement method and J-integral energy release rate to compute the stress intensity factor at each node. After these calculations have been performed, the Paris law, as described earlier, is used to calculate the distance of crack extension. Care is taken in assembling the model; special concern is given to the mesh mismatch at the boundary between the coarse uncracked portion of the model and the cracked block. The mesh mismatch is mitigated by the use of the 'multi-point constraint' method. Using the Paris law, the post-processor advances the corner nodes of the crack front elements exactly to their new positions. Remaining crack front nodes are then approximately fit using a cubic spline curve; this can guarantee that the nodes are spaced properly. In their research, Lin and Smith have found that a cubic spline gives much smoother results than using a series of straight lines to connect the crack front nodes [5].

To study how accurately their method works, [10] compares the numerical results of Lin and Smith with analytical solutions by Newman and Raju and various empirical results. Figures show originally elliptical and circular crack fronts propagating through a finite thickness specimen in tension, bending, and a combination of the two. Most interesting are the results that show elliptical crack fronts evolving into circular cracks under tensile loads. Overall, the crack propagation method utilized in articles [5, 10, and 11] by Lin and Smith seems to produce realistic results that compare favorably with others. The main weakness of this scheme is that it can only be applied to problems with mode I stress intensity factors. Therefore, only cracks in tension and bending can be studied, mixed-mode and interface cracks cannot.

In [12], O'Donoghue et al. investigated crack propagation using the finite element alternating method (FEAM) developed by Atluri and others and implemented with 2D and 3D versions in a program called SAFEFLAW. The FEAM solves the crack problem using two solutions, an analytical solution for an embedded elliptical crack in an infinite body and a finite element calculation of the stresses in the uncracked body. Using an iterative algorithm, the stress intensity factors are calculated along the crack front. The primary benefit of FEAM over traditional techniques is that it is relatively efficient; rather than a highly refined model of the crack front or the use of enhanced 'crack tip elements', a standard finite element analysis can be performed on a coarser mesh using fewer number of elements by roughly an order of magnitude. The stress intensity factor at each node is computed by summing those computed over the required iterations, usually four or five. In addition, the authors claim that FEAM can calculate mode I, II, and III stress intensity factors accurately, although only mode I is demonstrated in [12]. O'Donoghue et al. examined the application of FEAM to various aircraft components. Instead of determining numbers of cycles, the results are in the practical units of 'equivalent flight hours' to failure. Specifically, this team examined the fatigue propagation of three partially elliptical cracks in a countersunk rivet hole and a quarter-elliptical crack emanating from a weep hole in a vertical riser [12].

The Element Free Galerkin (EFG) method, as described by Krysl and Belytschko in [13], uses a variation on the finite element method. Instead of elements in the vicinity of the predicted crack front, there is an 'EFG superelement' which is divided into hexahedral 'background' elements, with only nodes placed within this region. A drawback is that solving the equations within the EFG superelement becomes more computationally expensive. Stress intensity factors are used to drive the crack front once 'advance vectors' are calculated. Flat triangles are used to represent the crack while straight-line segments represent the crack front. Once the edge of the specimen has been reached, the program trims and modifies the directions that future crack advances can make. If the crack front triangles grow beyond geometric bounds set for them, the adaptive meshing algorithm can divide or combine these triangles to maintain their desired sizes [13].

Using EFG, idealized cracks have been studied to compare results with theoretical findings. These include an inclined through crack, an embedded penny-shaped crack, an inclined, internal, penny-shaped crack, and a straight through crack in a rectangular bar loaded in tension and torsion. The results of each of these simulations can be compared to expected solutions. A comparison is made between the Modes I, II, and III stress intensity factors for the embedded penny-shaped crack and those predicted analytically. Since energy release rates are used in crack propagation, the EFG method can be used in mixed-mode problems. After each crack advance, a new mesh in not needed; only the shape functions must be modified due to changes in the nodal supports. Another positive feature of this method is that it allows for non-planar crack growth; results for each of Krysl and Belytschko's simulations show 'wavy' (non-planar) crack surfaces similar to those seen in real-life fatigue failures [13].

In his work, Galdos [14] calculates crack extensions by using energy release rates computed using the crack-tip contour J-integral, which has been converted into a volume domain integral. After calculating the energy release rates along the edge of the crack, the crack growth scheme is implemented. This starts by using the following equation

$$V(s) = \alpha\left(\frac{G(s)}{G_c}\right)^{\beta} \tag{16}$$

where s runs along the crack front, $V(s)$ and α have dimensions of velocity, β is a material property, and G_c and $G(s)$ are the critical and point wise energy release rates, respectively [14]. Using the velocity, each crack-tip extension is calculated over a given time, similar to Equations 2 and 3, with time, Δt, as the independent variable instead of the number of cycles, ΔN.

Galdos has applied his research to the solution of a finite cylindrical body with a circular crack or a semi-elliptical crack in a block of material. Circular crack results very closely mirror those predicted by Bentham, whereas the semi-elliptical crack results were consistent with the results computed by Newman and Raju. Although Galdos claims the method used in [14] can be applied to interfacial problems, it is not demonstrated in this article. The bimaterial crack cited in the title refers to crack advancement that takes place within a single material. In this case, the crack advances on a plane perpendicular to the interface; this advancement is meant to study the development of a crack as it approaches an interface [14]. Overall, the method described by Galdos seems adequate, although using the elapsed time instead of a number of loadings seems to unnecessarily add an extra variable.

In a very different analysis technique than the finite element codes mentioned above, BEASY (Boundary Element Analysis SYstem) uses the dual boundary element method (DBEM). BEASY is boundary element software that includes both a meshing algorithm and an analysis package. As explained in references [15], [16], and [17], DBEM computes both the stresses and displacements by using a special 'dual' element. An advantage of the boundary element method is that it requires only the surfaces, exterior and crack faces, to be meshed as opposed to the entire domain required for finite elements. This allows for the insertion of a crack, with its mesh, into a model where mesh refinement alone will be necessary [16]. Some drawbacks of the boundary element method (BEM) when compared to the finite element method are that it can be used only for certain linear problems, the BEM produces more difficult element integrals, and the BEM is considered an order of magnitude more difficult to implement [18].

BEASY can calculate mode I, II, and III stress intensity factors for embedded, surface, and interface cracks [17]. From these computed values, a K_{eff} is compared to a threshold value K_{th}, and if K_{eff} is greater, the crack will advance. K_{eff} is calculated as shown in Equation 17 [15]

$$K_{eff} = \sqrt{\left(K_I + \left|K_{III}\right|\right)^2 + 2K_{II}^2}\,. \tag{17}$$

This equation is then substituted for ΔG in Equation 4. The direction and size of the crack extension are then computed with an incremental crack surface; the calculations are then performed to determine the number of loads required for that extension. An advantage of this method is that with each iteration of the crack advance algorithm, the program adds another layer of elements to the crack front and then computes if refinement is needed; if so, more elements are added [16].

There are simple test cases such as a cylindrical tensile case and a non-uniformly loaded square case. BEASY has also been used to calculate the growth of an embedded semi-circular crack near the base of a gear tooth, in a crankshaft, and in the delamination of a section of patched aircraft skin. In the gear tooth and crankshaft simulations and in the non-uniform loading cases, the crack propagates in a non-planar manner, a very attractive feature possible with the BEASY simulation package [15, 16].

Investigators at Cornell University including Wawrzynek and Ingraffea are using a FRacture ANalysis Code for arbitrary, non-planar 3D crack growth (called FRANC3D) to study automated 3D fracture problems [19, 20, and 21]. FRANC3D, a program that can create either boundary or finite element meshes, stores topological information about the solids rather than geometric information because this allows for improved accuracy. Propagation can be performed on one (or more) non-planar cracks simultaneously, and criteria for crack development are calculated node by node, rather than by averaging as is done with software such as NASCRAC or NASA/FLAGRO also examined in [21]. The topological representation in FRANC3D requires the use of a 'tear' operator to separate volumes, planes, lines, and vertices when a crack propagates through them. FRANC3D predicts the location for the crack tip nodes and it then creates new edges there. Each node is advanced based on the *ΔK*, the stress intensity factor. Next, logic algorithms use loops to combine new nodes and vertices into elements which are then connected to the existing crack surfaces [19]. Furthering this work, a large group of researchers is examining running simulations on parallel processor clusters to greatly reduce run times [20]. To verify the FRANC3D simulation results, [19] and [21] present comparisons to NASCRAC and NASA/FLAGRO as well as experimental results. The accuracy of the reported results varies depending on the test, but the shape at failure is very accurately predicted by FRANC3D. In both [19] and [21], the solutions discussed involve only mode I stress intensity factors for both planar and non-planar cracks. No mention is made of FRANC3D capabilities to solve mixed-mode or interface problems.

3.0 Material Properties

On a bimaterial interface, the inherent variation in the materials causes crack initiation and propagation due to the mismatch of the thermal expansion between the materials. The materials have dissimilar coefficients of thermal expansion, and to create stresses within the model, a temperature change need only be prescribed. In semiconductor packaging, one of the critical interfaces is a silicon/epoxy boundary. The differences between the material properties of silicon and typical epoxy underfills are drastic, with Young's modulus varying by an order of magnitude and up to 20% difference in Poisson's ratio.

Developing polymers for electronic packaging applications has been vital to the continuing advancement of the microelectronics industry. These polymers have many uses including as photoresists for microlithography and as an insulating dielectric material in chips, in displays, and in interconnects. In the simulations cited here, the underfill material used was benzocyclobutene (BCB). BCB is a low-dielectric-constant (low-k) polymer developed for microelectronic packaging and interconnects. This epoxy (DOW Chemical trade name CYCLOTENE™) has become widely used because of its favorable qualities: low dielectric constant, low electrical current loss at high frequencies, low moisture absorption, low cure temperature, high degree of planarization, low level of ionic contaminants, high optical clarity, good thermal stability, excellent chemical resistance, and good compatibility with various metallization systems [22].

A BCB/silicon bond was used in this study because it is the only microelectronics material interface known to have fatigue crack growth characterization using the Paris law (Equations 1-4) parameters necessary for the type of simulation performed here. Snodgrass et al [6] have investigated the fatigue failure of BCB/silicon bonds bonded with a CYCLOTENE™ polymer resin. Their results are presented in Table 1 [6]. The values of C and m presented correlate to the interface bonding constants found in Equation 4, above. Material properties for these simulations were assumed isotropic because of the increased difficulty associated with anisotropy. In addition, any temperature dependent behavior of silicon, epoxy, or the interface bond has been simplified to these two parameters.

Snodgrass et al [6] fabricated their specimens using a BCB-type polymer (CYCLOTENE™ 3022-35, Dow Chemical Co.) sandwiched between two silicon substrates with native oxide surfaces. The tests performed with these specimens included a dual cantilever beam with tensile loadings on the top and bottom surfaces. Specimens tested in this manner determined only the mode I stress intensity factors and the related strain energy release rate. Other tests were carried out using a 'mixed-mode delaminating beam' where a beam in four-point bending was given a 'pre-notch' through the center of the top silicon layer. An initial crack length was also introduced [6]. Unfortunately, the mixed-mode tests carried out here only accounted for mode I and II fracture. It is also possible, that the total strain energy release rate, when mode III is included, would be higher than that computed by either of the tests performed in [6].

Silicon is a commonly used material with well-defined material properties. Polymers are not as easily defined, since each can have very different characteristics. Table 2 displays the material properties of silicon and BCB.

4.0 Static Results

4.1 – Finite Element Modeling

In this research, a finite element program called FRAC3D was used. This finite element software, developed at Lehigh University, uses the enriched element formulation that is described in detail in [23] by Ayhan and Nied. An advantage of this method is its versatility; enriched elements can be applied to arbitrarily curved crack fronts in a straightforward manner. Other capabilities of this method include interface cracks and cracks in orthotropic materials. Accurate calculations of stress intensity factors and strain energy release rates are essential to eliminating a large source of error in fatigue life predictions. Previously results from FRAC3D [23, 24] have been compared to known analytical solutions. In each case, the finite element results have compared favorably with the analytical solution with maximum error of a few percent.

In this study, the finite element model is formed by a macro using the ANSYS Parametric Design Language (APDL). First a material is selected, either silicon or the BCB polymer. Then, the line of the crack front for the initial step is defined. Next, two areas are created, one with the crack front and one that is the uncracked interior of the model. Each of these areas is extruded to form a volume. The lines surrounding the crack surface are duplicated and attached to the original crack front. These lines form another area. This new crack surface and the original uncracked area are extruded in the direction opposite that of the previous extrusion. This new portion is given the material properties of the second material. Finally, these four volumes are meshed.

A finite element mesh of one of the models can be seen in Figure 5. The model consists of four volumes and is composed of two materials, silicon in blue, and the BCB polymer layer in red. Top views in red will show the polymer layer. Typically, including for the results shown here, the model is run with the width and depth, 'W' and 'D', dimensions equal to each other with a value of 0.05. T_1 and T_2, the thickness of the epoxy and silicon layers, are set equal with a value of 0.01. The x- and y-axis lengths of the cracked surface, 'a' and 'b' respectively, are generally set equal with a value of 0.004, to form a symmetric crack front. Since the model is parametric, new values for these parameters can easily be specified with each new execution of the algorithm. The values above length units of meters, which means that the crack starts with lengths of 4 mm on each axis.

The two beginning crack shapes that were studied, shown in top view, are a quarter-circular corner crack shown in Figure 6a and what will be called a fillet-shaped corner crack, shown in Figure 6b. A side view showing the two materials and the level of refinement at the crack front and along the interface is shown in Figure 7. All volumes are meshed using 20-noded brick elements. Both the circular and fillet shapes have equal numbers of nodes and elements because the method which creates the finite element models divides the lines into equal numbers of sections each time it is executed. In ANSYS, the volumes are meshed using the VMESH command for the uncracked volumes; for volumes with crack faces, a sweep mesh is used (the VSWEEP command in ANSYS). After examining numerous cases, it was found, for both types of crack fronts, that the number of crack-front elements is critical to the accurate calculation of smooth strain energy release rate results. In order to obtain the greatest level of crack tip refinement and resolution, 40 elements were placed along the crack front. The integration order of the crack front enriched elements is critical in calculating accurate results, therefore high integration orders from 32 – 40 were used.

Because of time requirements for running the models, it was found to be impractical to use a large number of elements within the cracked block. Running FRAC3D on a model of 19,200 elements and 84,665 nodes on one processor of a multi-processor Unix workstation required approximately 3 hours per iteration (the mesh of this model can be seen for the quarter-circular crack in Figure 5). Over a 20-iteration simulation, such a run time was deemed unacceptable. No significant changes in the results were observed when the size of the model was reduced to 5600 elements and

26,317 nodes while maintaining 40 elements along the crack front (these are the meshes shown in Figure 6).

In its current state, the crack propagation algorithm has no provision for crack front refinement as the crack front grows. This means that as a crack advances and becomes longer it will always have the same number of crack tip elements. Also, for accurate results to be calculated along the free surfaces, a high degree of refinement is required at these locations. Adaptive mesh refinement also has not been incorporated into the current meshing algorithm performed in the APDL.

All post-processing of the finite element results from FRAC3D has been performed in MayaVi (version 1.3), free scientific data visualization software (available to download at http://mayavi.sourceforge.net). Advantages of MayaVi are that it runs on most operating systems and has a straightforward graphical user interface.

4.2 – Results from the First Step

Figure 8 shows the normalized stress intensity factors along the interfacial crack front for the quarter-circular corner crack when subjected to a -10°C uniform temperature change. In both models, symmetry boundary conditions have been placed on the two bimaterial surfaces that the crack front does not intersect (x-z and y-z planes). Essentially the model simulates a bimaterial block with four identical corner cracks; only one is shown. It can be seen in Figure 8 that each of the stress intensity factors is relevant in calculating the total G because their magnitudes are comparable; $\hat{K}_{II}$ has the greatest magnitude between approximately 10° and 80° resulting in high magnitude phase angles, $\hat{\psi}_L$, (> 60°). The results here can be compared to those in [3], although the signs of $\hat{K}_{II}$,

K_{III}, and ε have changed. This is due to a change in the sign of ε due to switching the upper and lower materials. Including more crack front elements has led to the smoother curves presented here. Another conclusion that can be drawn from the figures is that for the thermal quarter-circular crack, shear behavior dominates the entire crack front.

The normalization is with respect to a flat, circular crack embedded in silicon subjected to a thermal stress defined by $\sigma_T = E_1\alpha_1\Delta T$, where E_1 and α_1 are the elastic modulus and the coefficient of thermal expansion in silicon, respectively (and the value can be found in Table 2). For these simulations, the arbitrary length constant, L, has been defined as the thickness of each of the materials, 10 mm. The normalizing K_{IT} is calculated using $K_{IT} = \frac{2}{\pi}\sigma_T\sqrt{\pi a}$; the a used is the distance from the origin to the crack front at the central node, 4 mm in the circular case and 1.97 mm for the fillet-shaped case.

For interface cracks, strain energy release rate determines the crack advance. The normalized quarter-circular crack strain energy release rates are shown in Figure 9. This graph includes multiplication by $(\Delta T)^2$, since G_{IT} depends on K_{IT}^2. This result indicates that the quarter-circular corner crack will advance most rapidly near the free surfaces and more slowly in the center. The effective stresses are plotted in Figure 10 for the side view and near the crack front with the warping scaled by 100 times. The first plot shows the warping of the entire structure while the second illustrates that the intersection of the crack front and the free surface is the region with the highest stresses.

Figure 11 and Figure 12 present data similar to that in Figure 8 and Figure 9; the difference is that the former are the results of the fillet-shaped crack. The graph in Figure 11a shows a significant decrease in the magnitude of K_{III} while $\hat{K}_I$ and $\hat{K}_{II}$ have become approximately equal in magnitude and almost constant. Due to these factors, the phase angles, $\hat{\psi}_L$ and $\hat{\varphi}_L$, fluctuate much less. Meanwhile, Figure 12 shows a normalized G with opposite trends of those seen in Figure 9.

With the general information gathered from these first strain energy release rate graphs, it is possible to draw general conclusions about an advanced crack shape. For the quarter-circular crack, the edges will propagate much more quickly than the rest of the crack front, while the middle of the fillet-shaped crack will advance faster than the edges. Figure 13 is a plot of the effective stresses in the fillet-shaped crack; most notable here are the highest thermally induced stresses along the crack front and around the perimeter of the interface.

In Figure 8 - Figure 12, the graphs are quite smooth. The general exceptions here are the three to five nodes closest to each edge of the plots, although Figure 8 and Figure 9 are the worst. Near these free surfaces, obtaining accurate stress intensity factor results is difficult without very high levels of refinement, which would have substantially prolonged simulation times. This study examines primarily the overall 'macroscopic' shape of the propagating cracks and is not overly concerned with these small fluctuations. However, this seemingly small problem prevented the automatic remeshing required for the smooth operation of the crack propagation algorithm because a few elements became too skewed and misshapen for ANSYS to permit the meshes to be used. To compensate for this, a curve-smoothing process was developed to extrapolate the curve over the last two elements, replacing the results from these nodes and elements. Therefore, the nodes and elements adjacent to the free surfaces are not those calculated directly from the stress intensity factors because those are unreliable.

5.0 The Propagation Algorithm

5.1 – Creating the Models

The work detailed in this study focuses on creating an algorithm that performs the tasks of creating and automatically advancing an arbitrary crack front using the finite element software ANSYS to generate the finite element mesh. Completing this task uses a newly developed macro that links the operation of multiple existing programs. The ANSYS parametric design language (APDL) is used to automate the ANSYS commands and to run various independent programs without having to exit the ANSYS software.

A cracked solid model mesh is created using commercial ANSYS finite element software. For more detail on this, see Section 4.1 – Finite Element Modeling. Crucial finite element and crack front information is written to data files that are used as input for FRAC3D, software developed at Lehigh for fracture mechanics studies. Ayhan and Nied provide an in-depth look at the workings of FRAC3D version 1.0; see [24]. The strain energy release rate results from FRAC3D are used in the Paris Law (Equation 4) to advance the crack front. A flow chart of the process, as explained here, is shown in Figure 14.

Before running the APDL macro, a small program called WRITERUN (Unix) or 'runfile.exe' (Windows) must be executed. This simple program produces a *.run file. Writing the *.run file requires the user to input the type of analysis to be performed (whether it is non-linear, thermal or fracture), the material properties, the type of enriched elements used on the crack front and other parameters of the problem to be solved [24]. Since the algorithm will use the same material properties and finite element settings during each iteration, the user must write this file before running the automated algorithm. Heffes has explained this procedure for a general case, a curved crack, and a straight crack in [25, 26, and 27], respectively.

The first step in a crack propagation problem is to create the geometry of the model with its initial crack. This is done quickly with the macro, as it requires inputs including the dimensions of the cracked block and the crack itself. Other preliminary data include meshing parameters, the necessary material constants, and, for thermal problems, the uniform temperature difference that will be applied. Next, ANSYS generates and meshes the solid model. Here boundary conditions and loads are applied to the model and an ending parameter is specified.

From ANSYS six files are required as inputs for the FRAC3D software. These files are lists of the following: the elemental connectivity for the complete model, the nodes in the specimen, the applied loads (both mechanical and thermal), the boundary conditions, the crack front elements and their connectivity, and the crack tip nodes. The first four list files can be written easily using commands directly available within ANSYS. With the crack front defined, lists of the crack front nodes and elements are written.

These files are exported from ANSYS and read into a program called CONVERT. This program combines the data from the six list files and creates a *.geo file with this information. This is a file, in ASCII format, that contains the ANSYS data, but its order has been configured for use in FRAC3D. To run thermal analyses, another simple program called UNITEMP is executed from within the ANSYS macro. This program writes a *.tem file that contains a list of nodes and the uniform temperature change that will be applied to them. For the models listed here, all the nodes were specified to undergo the same temperature variation.

Next, the algorithm begins running the FRAC3D finite element software, which calculates the stress intensity factors and the strain energy release rates for each node along the crack front. The files needed as inputs into FRAC3D software are the *.run, *.geo, and *.tem files, which give the required information for running the simulation. The next step in the algorithm is to take the strain energy release rate results calculated by FRAC3D and implement them into calculating a crack extension length for each crack front node. Strain energy release rates are calculated at each node, so the crack should advance smoothly. The appropriate form of the Paris Law, shown in Equations 2, 3, and 4, is applied here. Using these equations, the propagation distance is calculated for each node to move forward. After calculating the distance, the direction portion of the crack advance vector is determined. ANSYS outputs the slope of the crack front at each node. Using this information, the crack front nodes are moved normal to the slope of the crack.

After each step, the macro produces result files. One such file is the ANSYS database with the nodes and elements so the user can go back to see the exact shape of the crack as it progresses. This is also important for troubleshooting, identifying exact problems, and locating problematic regions. Another output is a file of the x and y values of the keypoints (nodes) along the crack front. This is helpful for recreating the crack shape at each step as well as verifying whether the expected symmetry has been maintained. Another set of results of primary importance is the crack size (x- and y-axis intercepts) and the number of loading cycles required to complete that distance of crack propagation. The slope of the crack front at each node is also written to a file to be used by ANSYS as mentioned earlier.

If the crack completes one of the termination criteria established earlier, the program stops. Such criteria include running through the macro a specified number of iterations, the crack reaching a determined length, the completion of a specified number of cyclic loadings, or catastrophic failure occurs, G_c is exceeded. If termination criteria are not met, the process repeats. In [13], Krysl and Belytschko suggest that the remeshing of a solid model must be automatic in order to incorporate evolving geometry and update a changing mesh. In this research, the mesh is cleared, and the geometry is deleted. The crack front location information for the next step is read in from the data files stored during the previous step. A new crack front is placed through the keypoints calculated earlier and a spline is used to fit a smooth curve through the keypoints of the new crack front. The entire structure is reconstructed and remeshed, and a new crack front is formed. In the method explained here, exterior dimensions of the cracked block are maintained by being specified directly in the APDL.

5.2 – Mathematics of Propagation

To propagate a crack, the proper form of the Paris-Erdogan fatigue fracture law, shown in Equations 2 and 4, is used. For cases where a single fracture mode is present, Equation 2 can be used. Mixed-mode loading requires the use of Equation 4. Assuming an interface crack, the first calculation needed for a new crack front is the calculation of strain energy release rates along the existing crack front. Next, assuming isotropic material properties, C and m will be constant at each node. Finite approximations must be made for the derivative terms, *da* and *dN*. Next, a finite value must be selected for Δa_{max}, and the equation solved as shown below,

$$\Delta N = \frac{\Delta a_{\max}}{C(\Delta G_{\max})^m}. \tag{18}$$

The ΔG used here is the maximum of any node along the crack front. Since all the values on the right hand side are known, a value is computed for ΔN. Finally, this ΔN remains constant while calculating Δa for the rest of the crack front nodes with the equation in this form,

$$\Delta a = \Delta N\left(C(\Delta G_i)^m\right). \tag{19}$$

Once a crack propagation length, Δa, has been calculated for each crack front node, the slope of the crack front is used to place exactly the next crack front location for that node. Over each step, the crack advances 0.0001 m (0.1 mm) normal to the crack front at a specified node; more on the selection of Δa follows.

6.0 Results

6.1 – Crack Propagation Results

The expected results of the crack front propagation algorithm are that a 'steady-state' for the strain energy release rates will be reached. This does not imply that the crack will stop growing; rather it means that the crack front shape has been determined assuming a uniform ΔG along the crack front under steady state conditions. The crack propagation results are presented in Figure 15 and Figure 16; they show the successive locations of the corner nodes for the quarter-circular and the fillet-shaped cracks, respectively. For the quarter-circular crack, this node is on the free surface while the fillet-shaped crack moves the central node. It can be noted that each step moves significantly farther than 0.1 mm. This is due to the sharp angles (< 45°) at which the crack fronts meet the free surface. For an intersection angle of 30° - 45°, it is expected, using simple trigonometry, that the crack must move along the x and y-axes at a rate between $\sqrt{0.02} = 0.141$mm and 0.20mm per iteration. Both of these figures also have a straight line connecting the nodes on the free surface of the final step. This is included to show clearly the curvature of the crack front. The finite element meshes are shown at the last step in Figure 17.

The final shape simulated here is similar to that seen in Figure 3 at the third step in the progression. It can be seen that both the quarter-circular and fillet-shaped cracks evolve toward a similar shape. Lin and Smith describe this tendency in [10] by saying an advancing crack "will grow towards a so-called preferred propagation path (PPP) that is related to the loading mode, whatever the shape of its initial defect. The rate of such a tendency towards the PPP is greater for a larger deviation between the current crack shape and the PPP." The faster growth rates can be seen during the first few iterations of the algorithm along the free surfaces in Figure 15 and near the center of the crack in Figure 16.

Another way to illustrate that a crack grows more quickly where the shape deviates the most from the steady-state shape is provided by Figure 18. Most notable about this graph is the very low number of cycles needed for the first four steps to begin smoothing the sharp corners of the quarter-circular crack. Other regions of interest are the last 13 steps of the fillet-shaped crack and the last 3 steps of the circular crack; both curves have become linear. The linear sections indicate that a 'steady state' has been reached. After reaching 'steady-state,' a similar shape will propagate with constant values of the strain energy release rate along the length of the crack front. The original shape of the crack front does not change the final crack front shape, and this can be seen by comparing the final shapes of the cracks.

The evolution of the strain energy release rates as the crack propagates is shown in Figure 19. In both plots, the initial shapes, as detailed earlier in Section 4.2 – Results from the First Step, correspond to 'Step 1'. Once a steady state has been reached, the strain energy release rates have become constant. Before normalization, these plots overlapped each other. When K_{IT} is normalized with the equation $K_{IT} = \frac{2}{\pi}\sigma_T\sqrt{\pi a}$, where a is the distance from the origin to the central node of the crack, the normalized $\frac{G}{G_{IT}}$ values decrease. As the G values approach a constant value, Figure 20 shows the normalized $\hat{K}_I$, $\hat{\varphi}_L$ and K_{III} plots flattening as the crack progresses while $\hat{\psi}_L$ and $\hat{K}_{II}$ maintain shapes close to those of the first step. In Figure 21, $\hat{K}_I$, $\hat{K}_{II}$, $\hat{\psi}_L$ smooth over time while K_{III} and $\hat{\varphi}_L$ do not.

It has been observed that decohesion of thin films on brittle substrates often initiates at the edge or corner of the specimen and propagates toward the interior on the interface. After extending for a length on the order of the film thickness, the crack is frequently observed to deviate into the substrate [1, 7]; the transition between interfacial cracking and kinking out of the interface was not accounted for in these planar crack models. In the simulations performed here, all cracks were forced to maintain their planarity and stay on the interface.

6.2 – Algorithm Variables

Selecting the crack extension rate per step, Δa_{max}, was initially done arbitrarily until it was found that there are acceptable bounds for what can be used. For reasonable results, the crack advance distance per step must be chosen appropriately. If a value for Δa_{max} is selected which is too small, the algorithm will produce large data sets, and each will reflect very little change in the model. Since running FRAC3D can take upwards of an hour per step, running the algorithm through many unnecessary iterations wastes computing power, storage space, and time. On the other hand, a value of Δa_{max} must be selected that is small enough so that oscillations do not occur. This happens when a curved section of a crack front has nearly arrived at its 'steady-state' configuration. Since the step taken by the algorithm is too great, previously concave sections of the crack front will become convex and vice versa; a 'smooth' crack front will be bypassed because of the large Δa_{max} value. While simulating crack growth, a value of Δa_{max} equal to 2.5% of the initial x or y-axis values was found acceptable while 5% or higher was not. For example, a symmetric crack with x and y-axis intercepts of 4.0 mm was found to advance smoothly with crack advancement steps of 0.1 mm.

The value of the temperature difference, ΔT, specified by the user during the beginning of the algorithm makes an enormous difference in the number of cycles computed. For example, using the values from Table 1, a calculation for decreasing the temperature difference by half, from 20° to 10° C, is detailed below. First,

$$\Delta T \propto \Delta K . \tag{20}$$

And with Equation 5, it follows that

$$\Delta G \propto \Delta K^2 . \tag{21}$$

Next, Equation 4 is rearranged, and two of them are set up as a ratio

$$\frac{dN_1}{dN_2}=\frac{\left(\dfrac{da}{C(\Delta G_1)^m}\right)}{\left(\dfrac{da}{C(\Delta G_2)^m}\right)}=\left(\frac{\dfrac{1}{\Delta G_1}}{\dfrac{1}{\Delta G_2}}\right)^m=\left(\frac{\Delta G_2}{\Delta G_1}\right)^m, \tag{22}$$

where C, Δa, and m are constant. In Equation 20, a decrease in the temperature difference, ΔT, by an order of 2 (with $m = 6.0$) will result in an increase in the number of cycles required to produce an equal distance of crack advancement, dA, of $4^{6.0} = 4096$ times.

6.3 – A Numerical Problem

Recent documentation on the use of FRAC3D software including the tutorials by Heffes [25, 26, and 27], explains the process for writing out the six files needed for running CONVERT and FRAC3D (see an explanation of this Section 5.0 The Propagation Algorithm). To write the needed output files, the following ANSYS commands are used: ELIST, for elements, NLIST, for nodes, and DLIST, to write the constrained degrees of freedom. Since these are similar commands writing out similar files, this seemed logical. Many months were spent struggling to get smoother crack fronts and strain energy release rate graphs were to no avail. It was then suggested that a command called NWRITE be used to define the nodal locations instead of the NLIST command. Results varied greatly each time the algorithm was run. The advantage of NWRITE is that the file it writes in double precision with nine significant figures rather than five. Upon running the algorithm the first time with the new command, the difference was noticeable. Instead of having to try, in vain, to smooth the stress intensity factors, the NWRITE results could be used without smoothing.

6.4 – Phase Angle (ψ) Investigations

Although few articles were found that quantify the effects of phase angle, it has been observed that lower phase angles lead to shorter fatigue life predictions due to the predominance of the more severe mode I stress intensity factor. Hutchinson and Suo summarized the previous work on phase angle and its relationship to interfacial fatigue life [7], but studies cited therein measured only the critical strain energy release rates, G_c. It is believed that the effects of a high phase angle will do more than increase the G_c for a bimaterial interface; it will also decrease the crack propagation rate, hence,

$$\frac{da}{dn} = f(G, \psi). \tag{23}$$

To model this most accurately, it has been conjectured that m (from Equation 4) must be modified and the resulting relationship looks like

$$\frac{da}{dn} = C(\Delta G)^{m(\psi)}. \tag{24}$$

The only data found in the literature to verify this hypothesis comes from Snodgrass et al. [6] where two data points were presented. On the interface they investigated, a phase angle, ψ, of 0° produces $m \sim 6$ and at a ψ of 43° results in $m \sim 4$. The $\psi = 0°$ was produced using a double cantilever beam test while $\psi = 43°$ was produced under the mixed-mode delaminating beam configuration (also called the t-crack bend specimen). Although more sophisticated equations could be postulated, it was assumed that a linear relationship between m and ψ is justifiable since fatigue data only exists for these two phase angles. The equation of a straight line through these two points (in radians) is

$$m(\psi) = 6 - 2.665|\psi|. \tag{25}$$

The results for the phase angle controlled crack propagation algorithm are plotted in Figure 22: Plot of the nodal points of the advancing quarter-circular corner crack. The straight line is to illustrate the curvature of the crack front.Figure 22, Figure 23, and Figure 24. Figure 22 depicts the growth of the originally fillet-shaped crack. When comparing this phase angle controlled graph to the results using only strain energy release rate, in Figure 15 and Figure 16, it can be seen that the edges propagate more rapidly in the phase angle controlled model than the central nodes. Figure 23 presents a comparison of phase angle and strain energy release rate results after 19 iterations of the propagation algorithm. Although it may look like the phase angle controlled graph advances much more rapidly, this is not the case because the m values (calculated with Equation 25) range from 2.9 to 3.5 as compared to $m = 6$ for the other simulations. This causes the phase angle controlled model to propagate approximately three orders of magnitude more slowly. The final plot, Figure 24 shows the change in the G_{total} over the advancement of the crack. When compared to similar graphs (in Figure 19), it can be seen that Figure 24 starts in a similar fashion to the fillet-shaped crack. The primary difference is that during the final propagations, the G values never approached a constant value as they did in the prior examples. Also, phase angle was found not to change greatly over the course of the iterations.

It was found that controlling the crack advance with the phase angle produced the following results. The crack edges propagated faster than the central nodes of similar shaped cracks. The crack propagated far more slowly than those using only the strain energy release rate, and phase angle controlled cracks evolved into different shapes.

Finally, the G-values never became constant for phase angle, as was seen when the strain energy release rate controlled propagation.

Table 1: Constants in the power-law growth-rate relationships obtained by fitting cyclic-fatigue debond growth rate curves. Results from the mid-range growth rates only [6].

Adhesion Promoter	C (J/m^2)	m	ΔG_{th} (J/m^2)
None	4.0×10^{-13}	6.0	3.4
Amino-silane	4.2×10^{-14}	6.2	6.1
Vinyl-silane	1.7×10^{-13}	6.1	7.0

Table 2: Material properties of silicon and benzocyclobutene (BCB) [22].

Material	Young's Modulus, E	Poisson's Ratio, υ	Thermal Expansion, α
BCB	2.9 GPa	0.34	5.2×10^{-5}
Silicon	128.28 GPa	0.279	2.6×10^{-6}

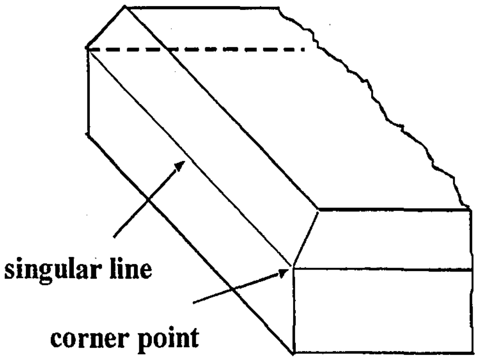

Figure 1: Locations of stress singularities on an interface between dissimilar materials.

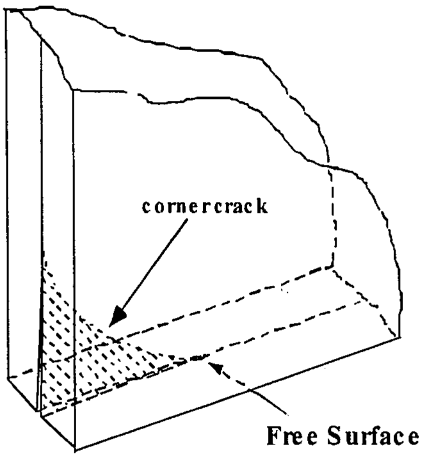

Figure 2: Depiction of an interface crack advancing along bond place between dissimilar materials.

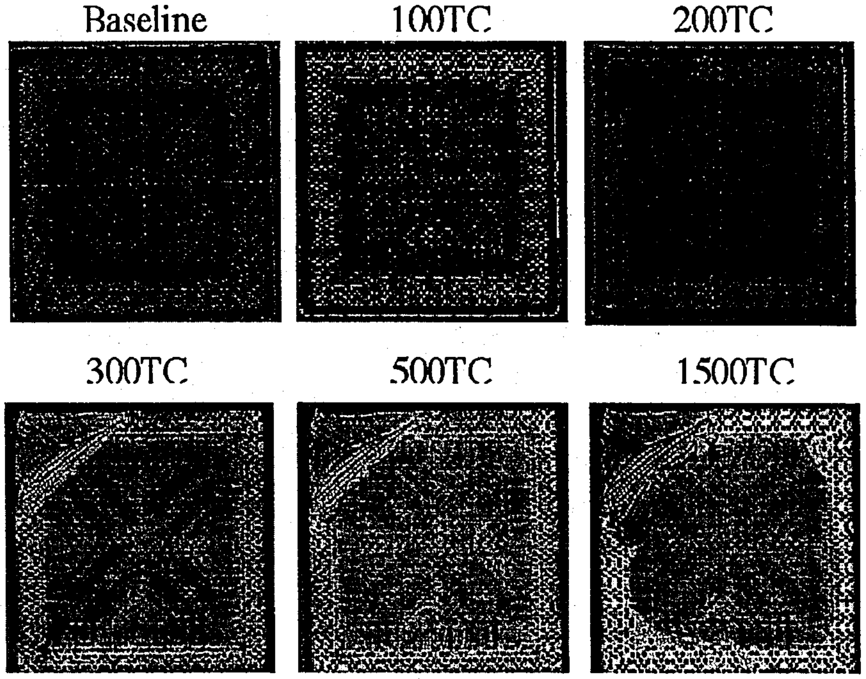

Figure 3: A series of C-SAM images of the progression of a corner crack at the interface between the silicon die and epoxy underfill in a flip chip package.

Note: TC means 'thermal cycles.' (Courtesy of David Peterson, Sandia National Laboratories).

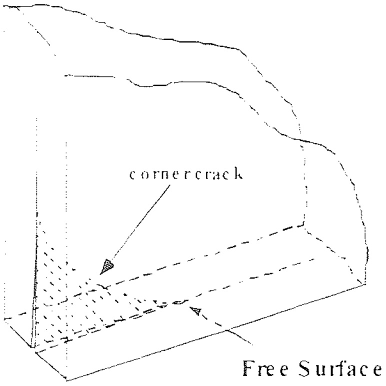

Figure 2: Depiction of an interface crack advancing along bond place between dissimilar materials.

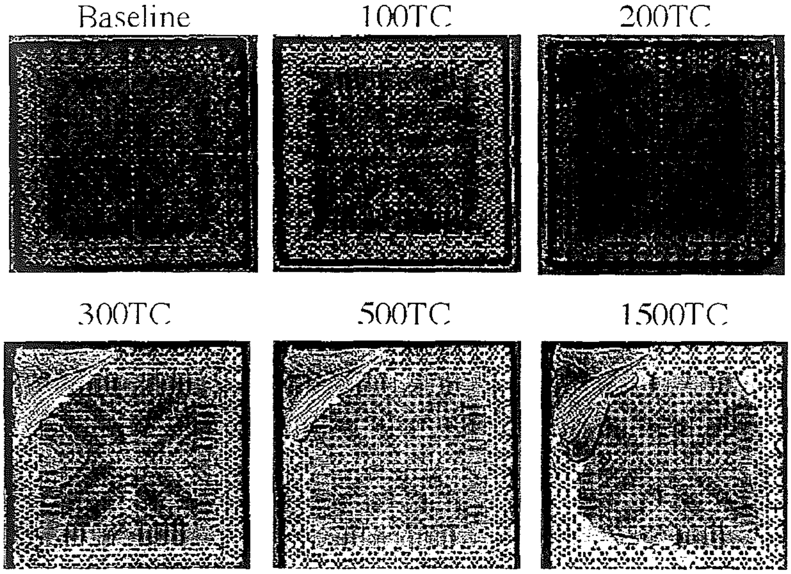

Figure 3: A series of C-SAM images of the progression of a corner crack at the interface between the silicon die and epoxy underfill in a flip chip package.

Note: TC means 'thermal cycles.' (Courtesy of David Peterson, Sandia National Laboratories).

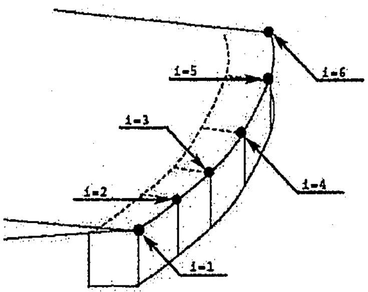

Figure 4: Stress intensity factors will be calculated along the crack front (i=1-6), as applicable to Equations 2 - 4.

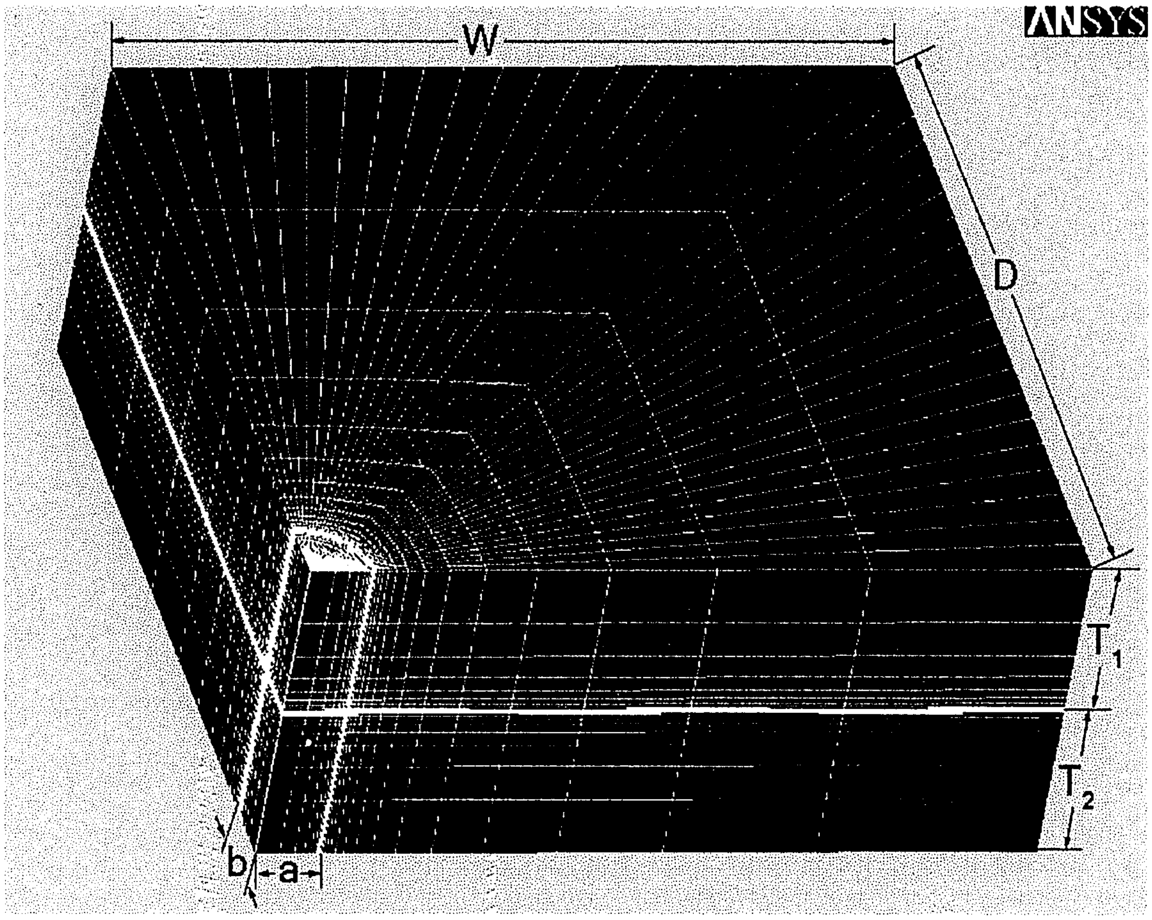

Figure 5: The finite element model used for the simulations.

The values for these parameters shown here are those typically used: D = W = 0.05, T1 = T2 = 0.01, and a = b = 0.004.

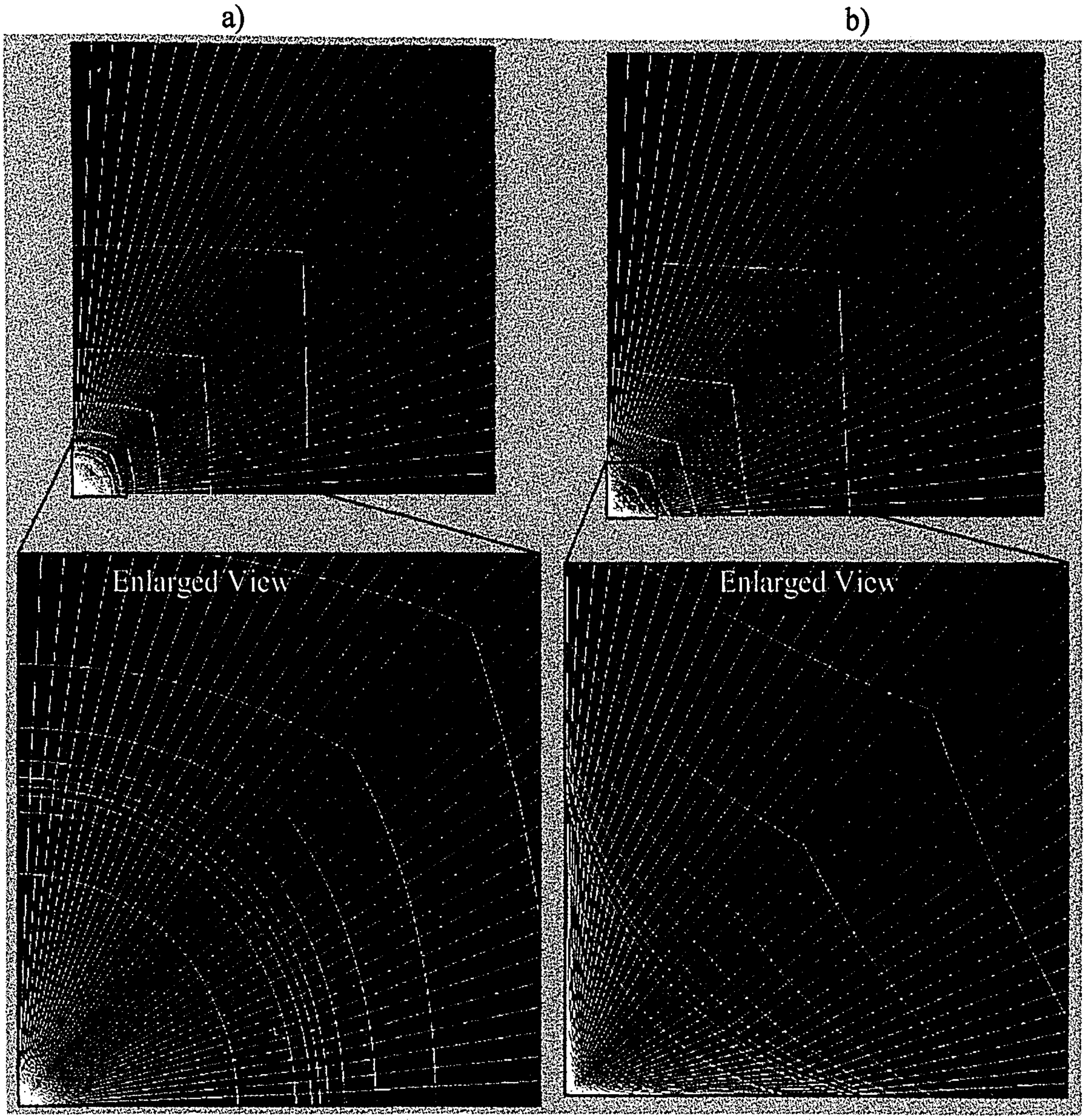

Figure 6: Top view and mesh of a) the quarter-circular corner crack and b) the fillet-shaped corner crack.

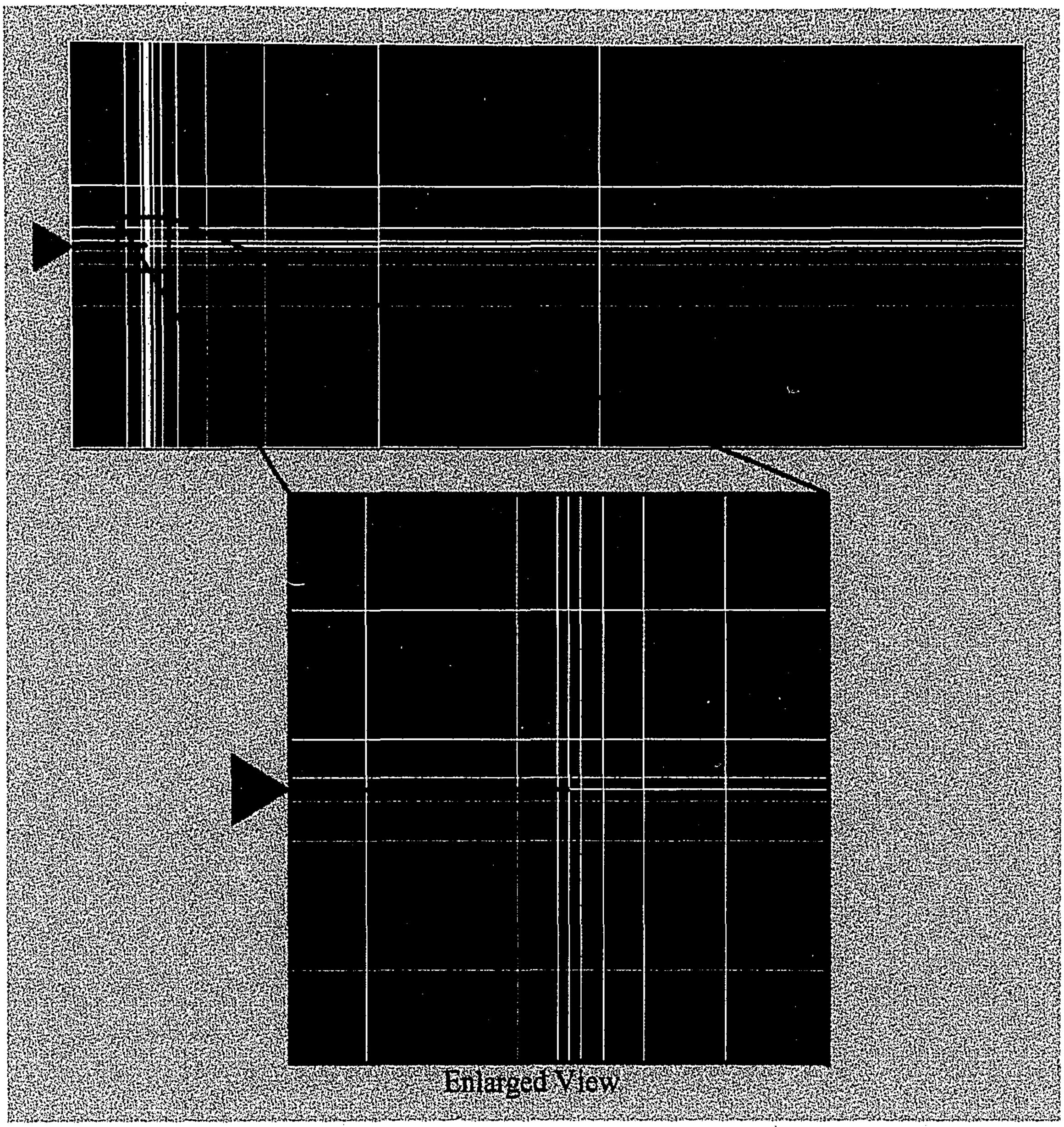

Figure 7: This shows the finite element mesh and the level of refinement at the interface and crack front. The internal black line denotes the crack surface.

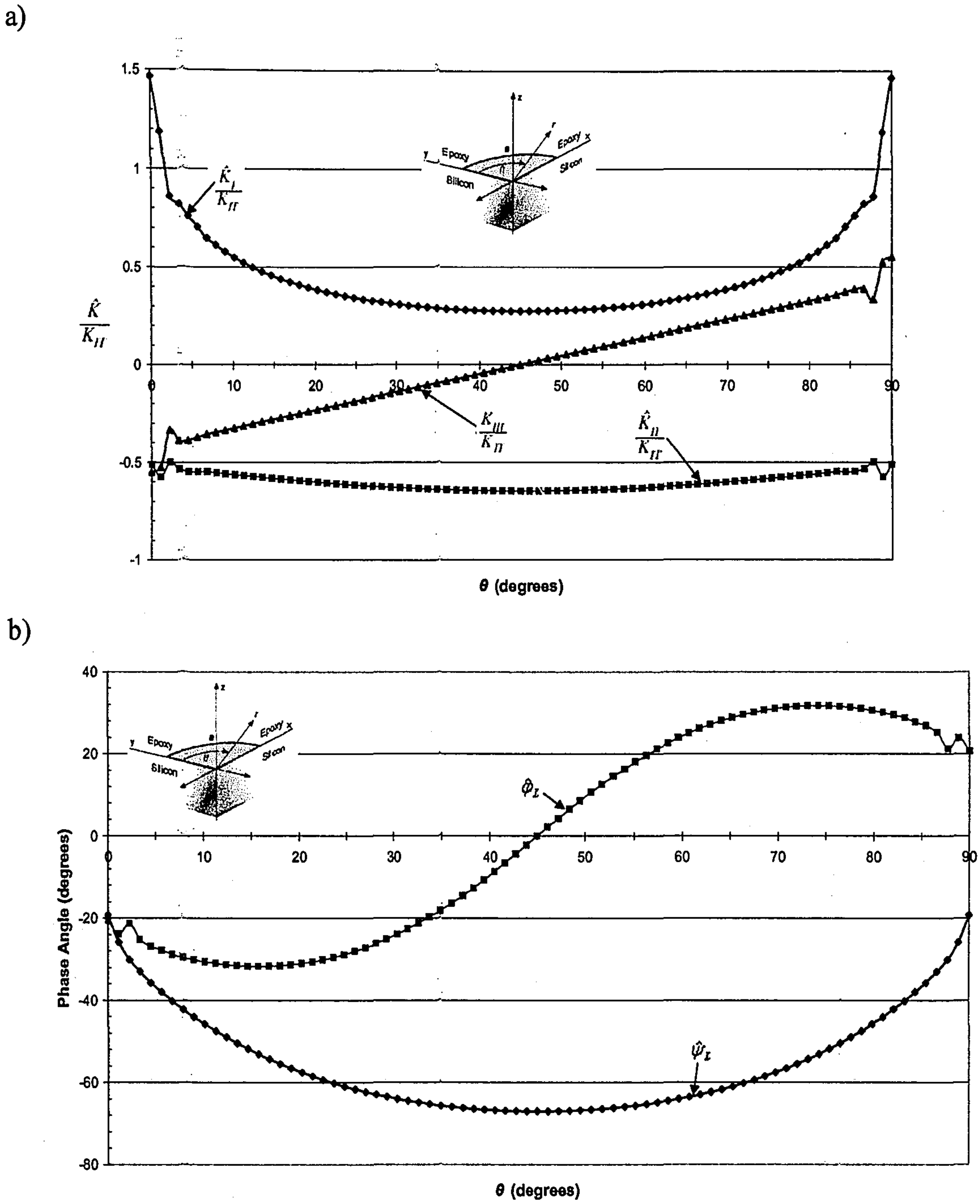

Figure 8: Step 1 results from the quarter-circular corner crack showing a) normalized stress intensity factors as a function of θ for a corner crack on a BCB epoxy/silicon interface subjected to a $-\Delta T$ (°C) uniform cooling and b) the normalized phase angles $\hat{\psi}_L$ and $\hat{\varphi}_L$.

Where $\hat{K}_I = K_I\cos(\varepsilon\ln L) - K_{II}\sin(\varepsilon\ln L)$, $\hat{K}_{II} = K_I\sin(\varepsilon\ln L) + K_{II}\cos(\varepsilon\ln L)$, **$\varepsilon$=-.0745,**

L=0.01m, $K_{IT} = \frac{2}{\pi}\sigma_T\sqrt{\pi a}$, $\sigma_T = E_1\alpha_1\Delta T$, **$\Delta T$=-10°,** $E_1\alpha_1 = 3.336\times10^5$,

$\hat{\psi}_L = \tan^{-1}\frac{\hat{K}_{II}}{\hat{K}_I} = \psi + (\varepsilon\ln L)$ **and** $\hat{\varphi}_L = \tan^{-1}\frac{K_{III}}{\hat{K}_I}$.

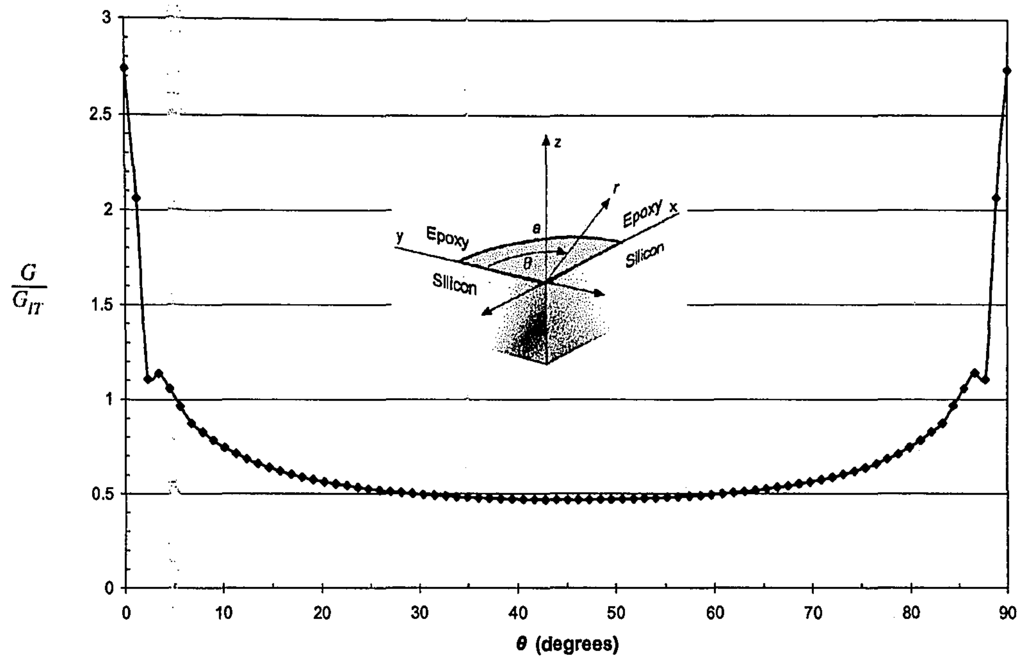

Figure 9: Step 1 normalized strain energy release rates as a function of *θ* for the quarter-circular corner crack on a BCB epoxy/silicon interface subjected to a $-\Delta T$ (°C) uniform cooling.

Where $G_{IT} = \frac{1}{E_0}K_{IT}^2$, $\frac{1}{E_0} = 1.56\times10^{-4}(MPa)^{-1}$, $K_{IT} = \frac{2}{\pi}\sigma_T\sqrt{\pi a}$, $\sigma_T = -E_1\alpha_1\Delta T$, ΔT=-10°, **and** $E_1\alpha_1 = 3.336\times10^5$.

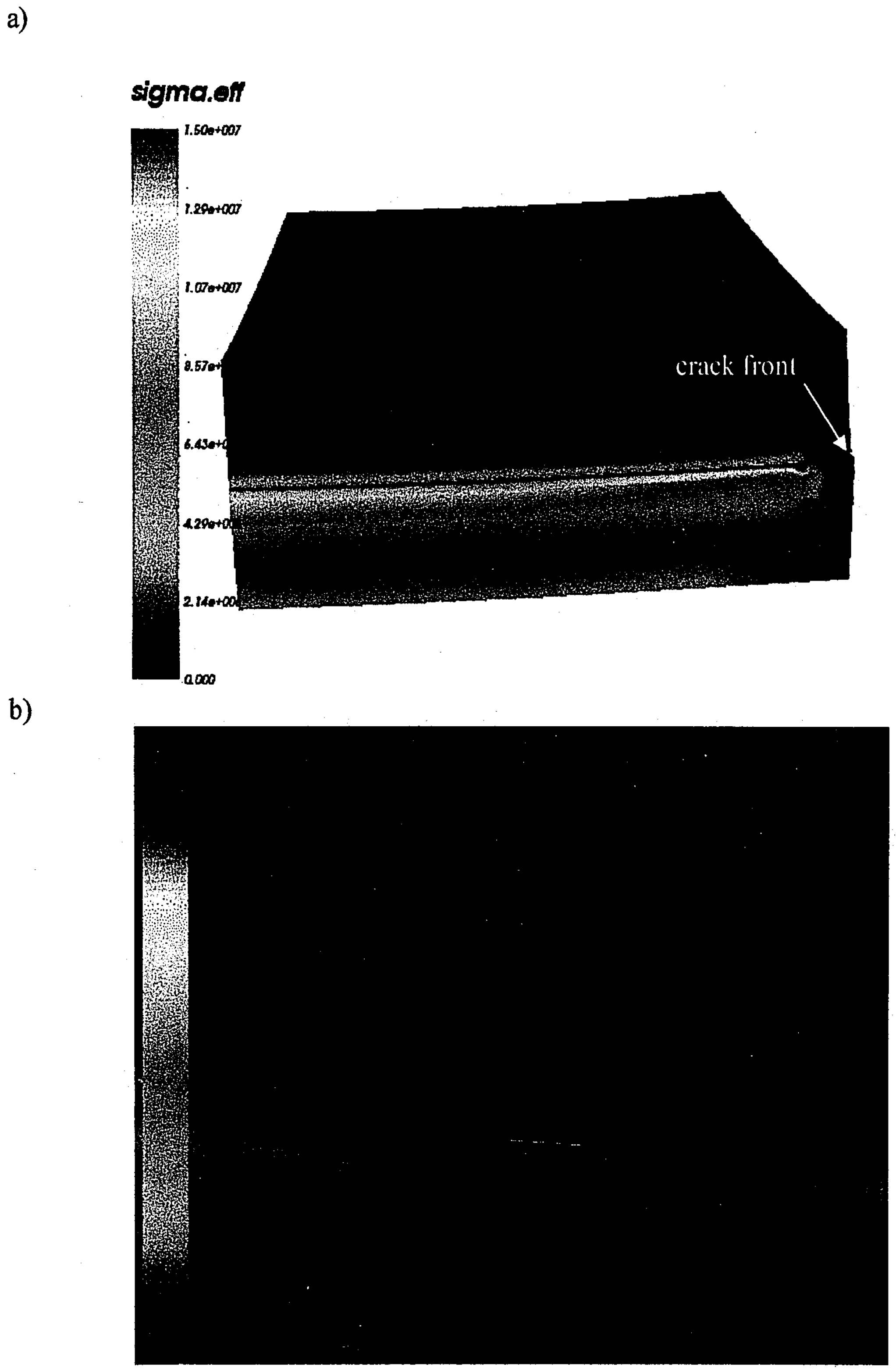

Figure 10: Plots of effective stresses in the quarter-circular crack a) from a side view and b) at the crack opening. Warping scaled by 100.

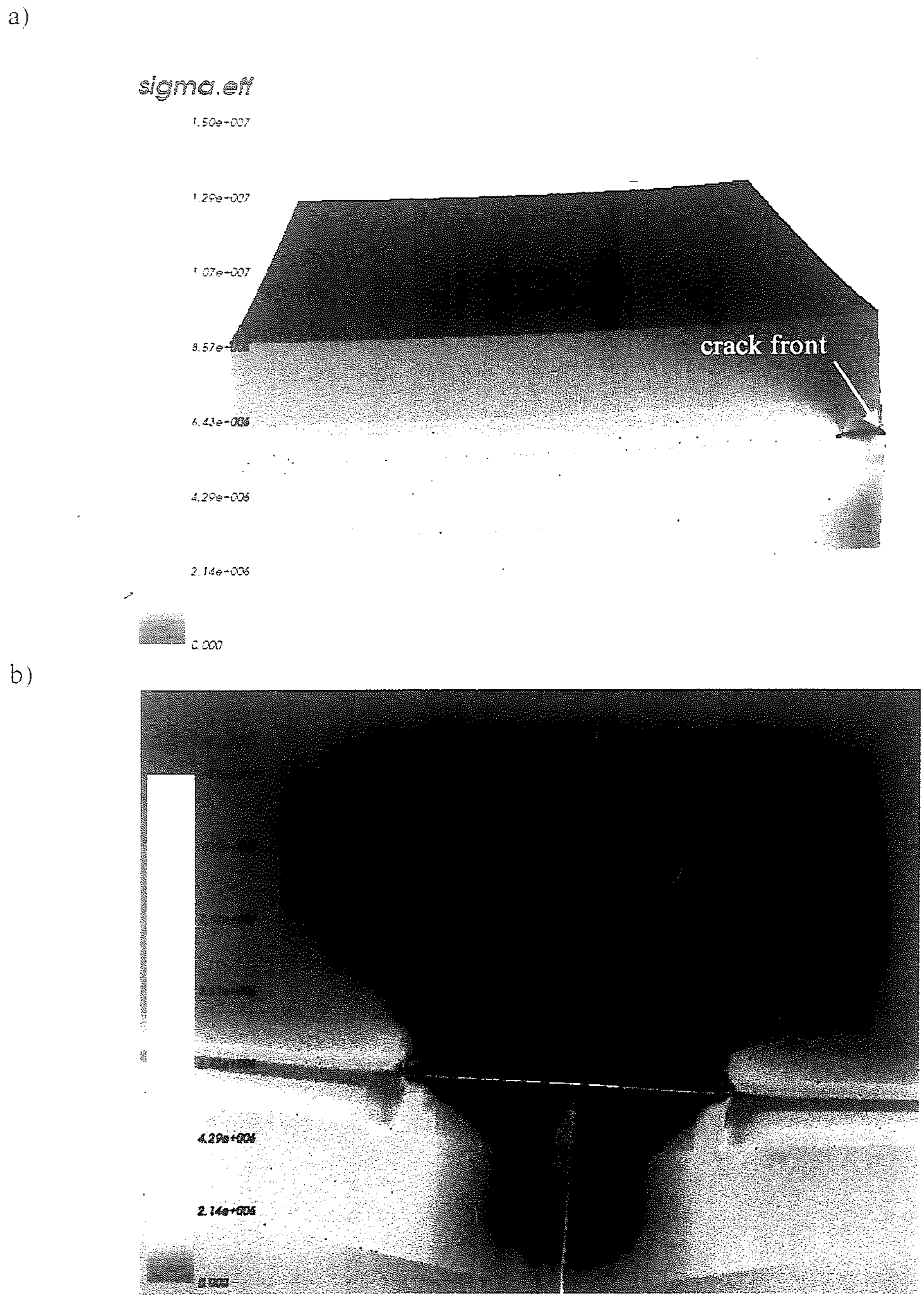

Figure 10: Plots of effective stresses in the quarter-circular crack a) from a side view and b) at the crack opening. Warping scaled by 100.

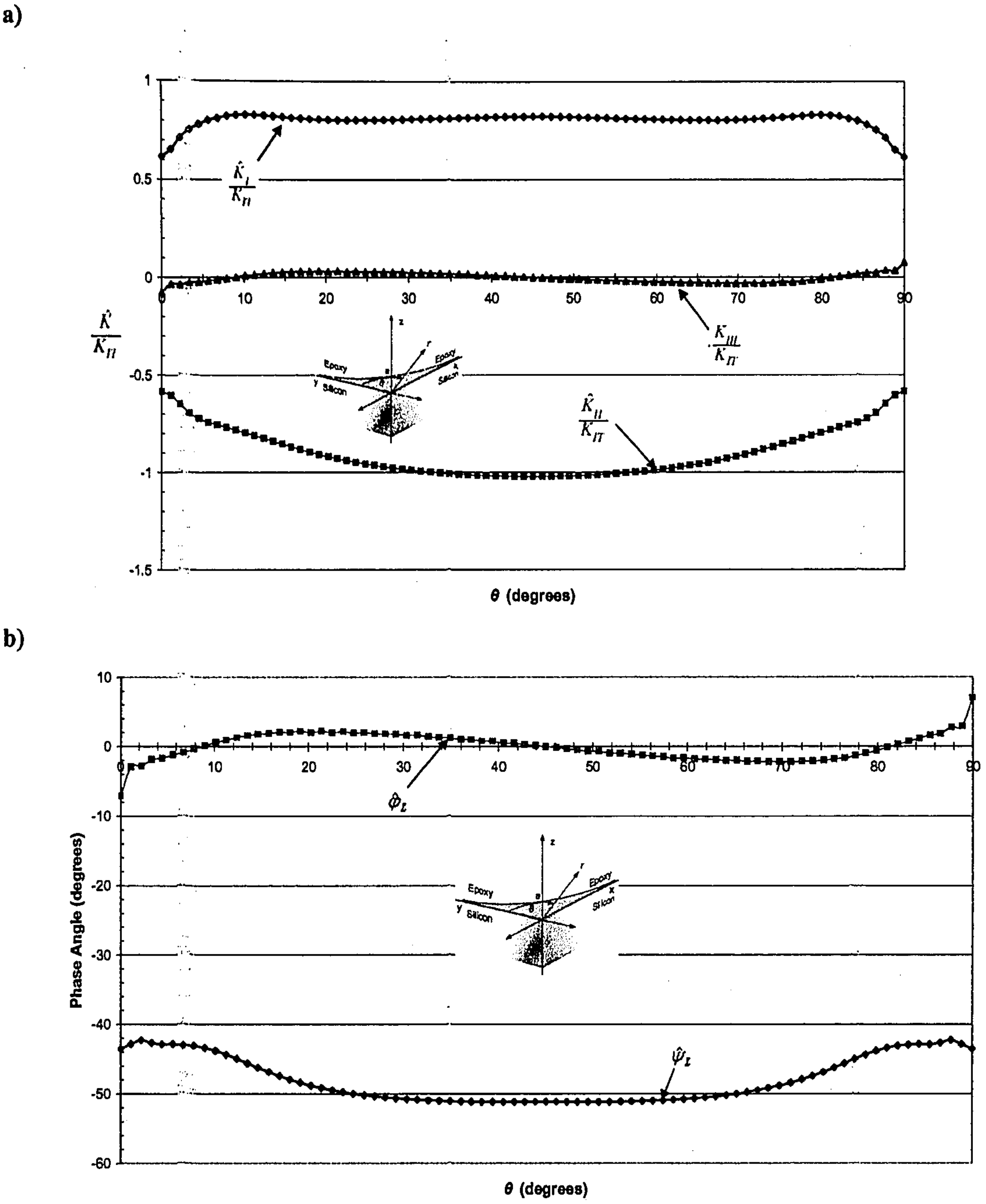

Figure 11: Step 1 results from the fillet-shaped crack showing a) normalized stress intensity factors as a function of θ on a BCB epoxy/silicon interface subjected to a $-\Delta T$ (°C) uniform cooling and b) normalized phase angles $\hat{\psi}_L$ and $\hat{\varphi}_L$.

Where $\hat{K}_I = K_I\cos(\varepsilon\ln L) - K_{II}\sin(\varepsilon\ln L)$, $\hat{K}_{II} = K_I\sin(\varepsilon\ln L) + K_{II}\cos(\varepsilon\ln L)$, **$\varepsilon$=-.0745, L=0.01m,** $K_{IT} = \frac{2}{\pi}\sigma_T\sqrt{\pi a}$, $\sigma_T = E_1\alpha_1\Delta T$, **$\Delta T$=-10°,** $E_1\alpha_1 = 3.336\times10^5$,

$$\hat{\psi}_L = \tan^{-1}\frac{\hat{K}_{II}}{\hat{K}_I} = \psi + (\varepsilon\ln L) \text{ and } \hat{\varphi}_L = \tan^{-1}\frac{K_{III}}{\hat{K}_I}.$$

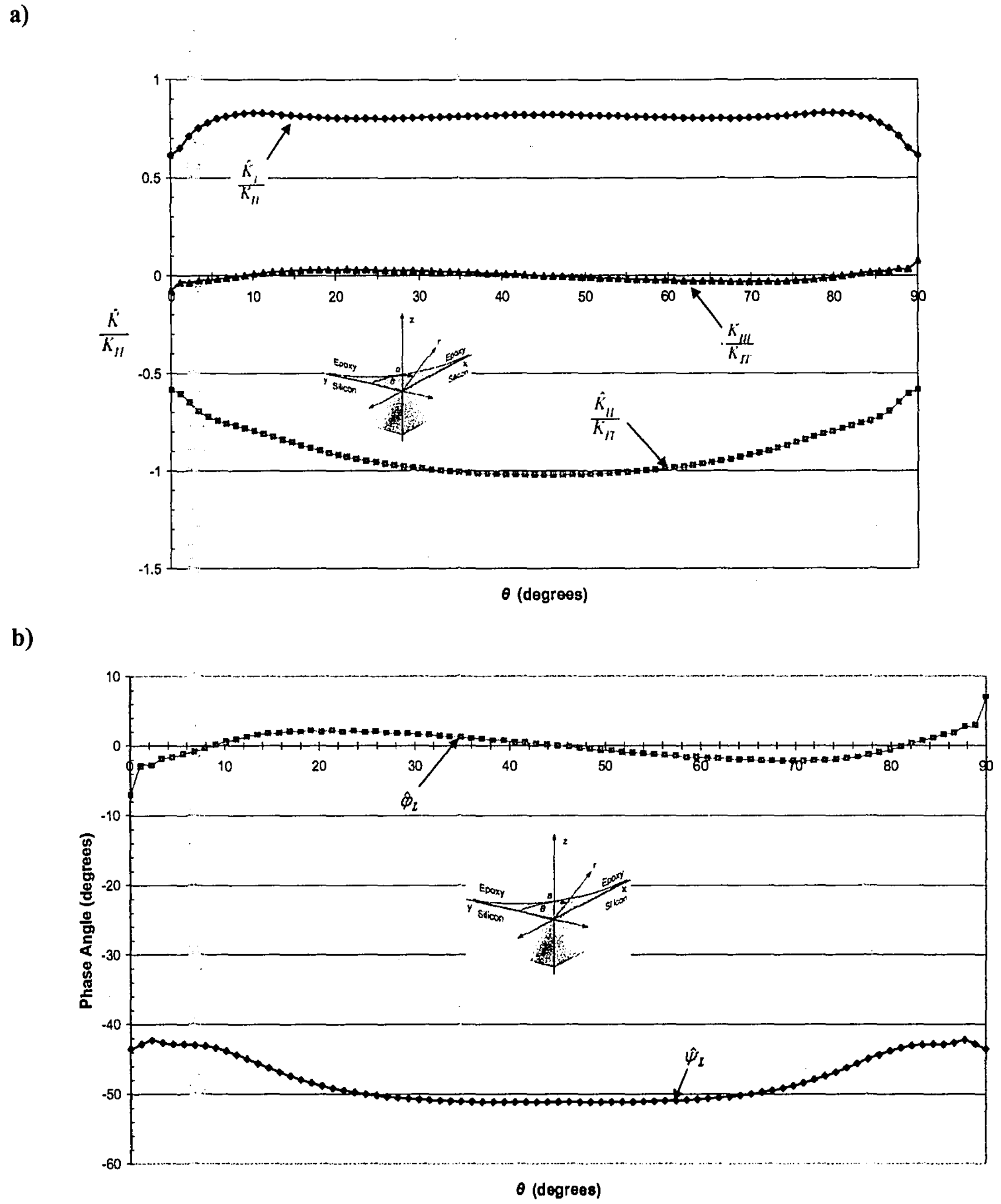

Figure 11: Step 1 results from the fillet-shaped crack showing a) normalized stress intensity factors as a function of θ on a BCB epoxy/silicon interface subjected to a $-\Delta T$ (°C) uniform cooling and b) normalized phase angles $\hat{\psi}_L$ and $\hat{\varphi}_L$.

Where $\hat{K}_I = K_I\cos(\varepsilon\ln L) - K_{II}\sin(\varepsilon\ln L)$, $\hat{K}_{II} = K_I\sin(\varepsilon\ln L) + K_{II}\cos(\varepsilon\ln L)$, ε=-.0745, L=0.01m, $K_{IT} = \frac{2}{\pi}\sigma_T\sqrt{\pi a}$, $\sigma_T = E_1\alpha_1\Delta T$, ΔT=-10°, $E_1\alpha_1 = 3.336\times10^5$,

$$\hat{\psi}_L = \tan^{-1}\frac{\hat{K}_{II}}{\hat{K}_I} = \psi + (\varepsilon\ln L) \text{ and } \hat{\varphi}_L = \tan^{-1}\frac{K_{III}}{\hat{K}_I}.$$

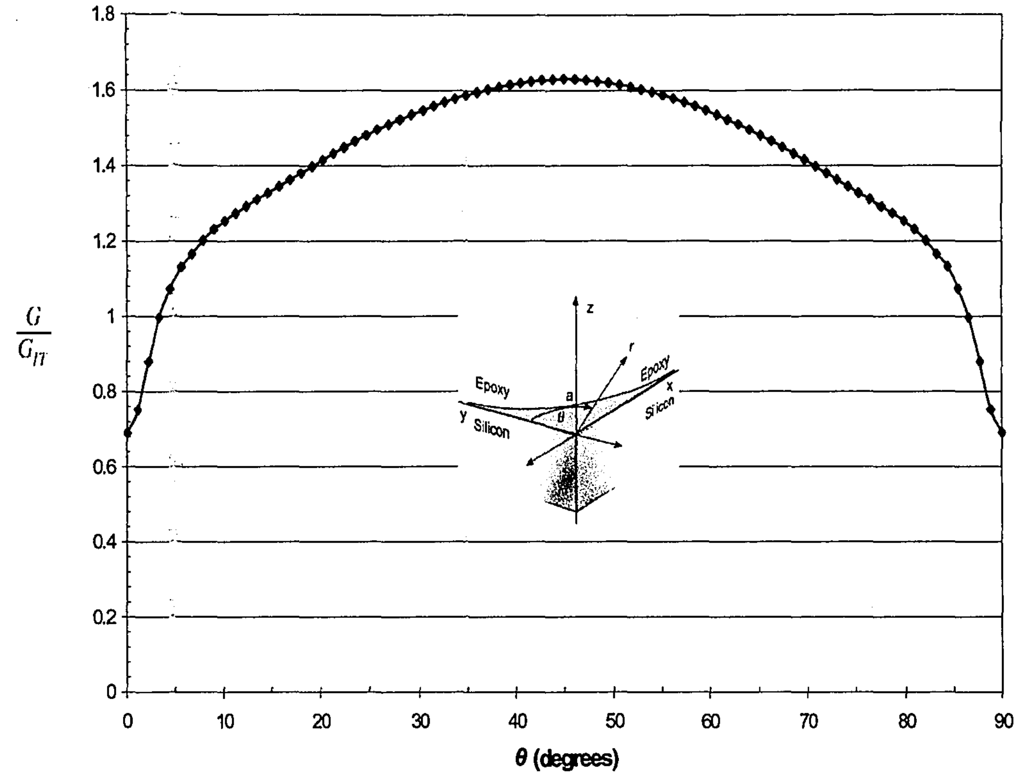

Figure 12: Step 1 normalized strain energy release rates as a function of θ for the fillet-shaped corner crack on a BCB epoxy/silicon interface subjected to a –ΔT (°C) uniform cooling.

Where $G_{IT} = \frac{1}{E_0}K_{IT}^2$, $\frac{1}{E_0} = 1.56\times10^{-4}(MPa)^{-1}$, $K_{IT} = \frac{2}{\pi}\sigma_T\sqrt{\pi a}$, $\sigma_T = -E_1\alpha_1\Delta T$, ΔT=-10°, **and** $E_1\alpha_1 = 3.336\times10^5$.

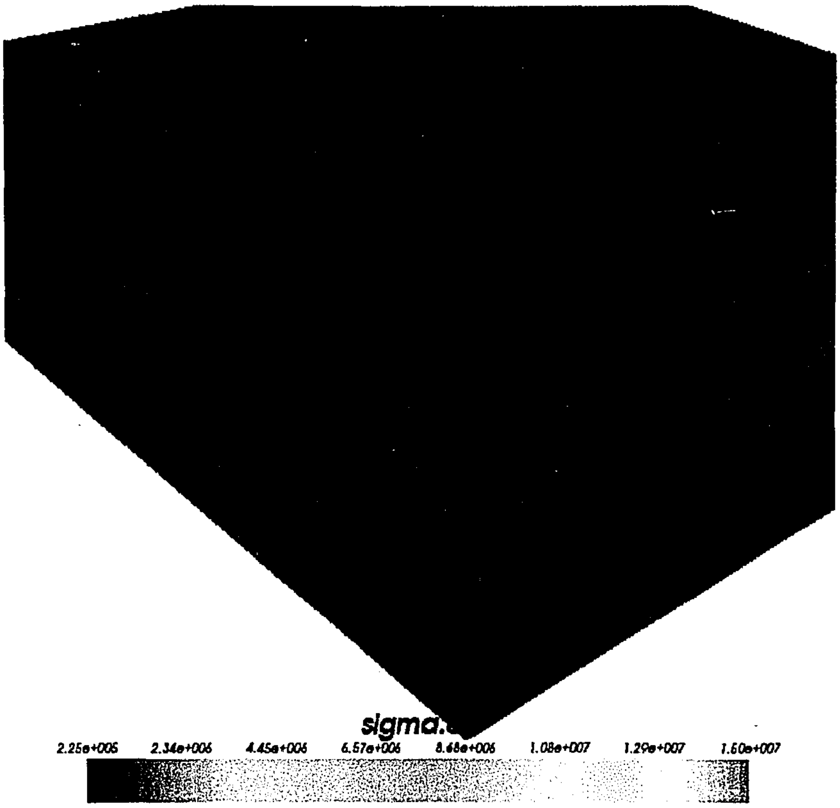

Figure 13: A plot of the effective stresses in the first step of the fillet-shaped crack.

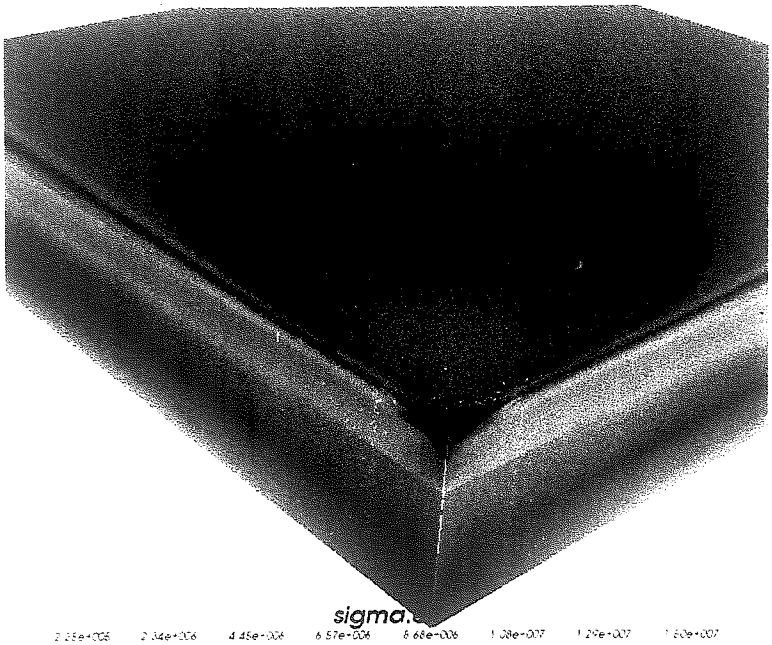

Figure 13: A plot of the effective stresses in the first step of the fillet-shaped crack.

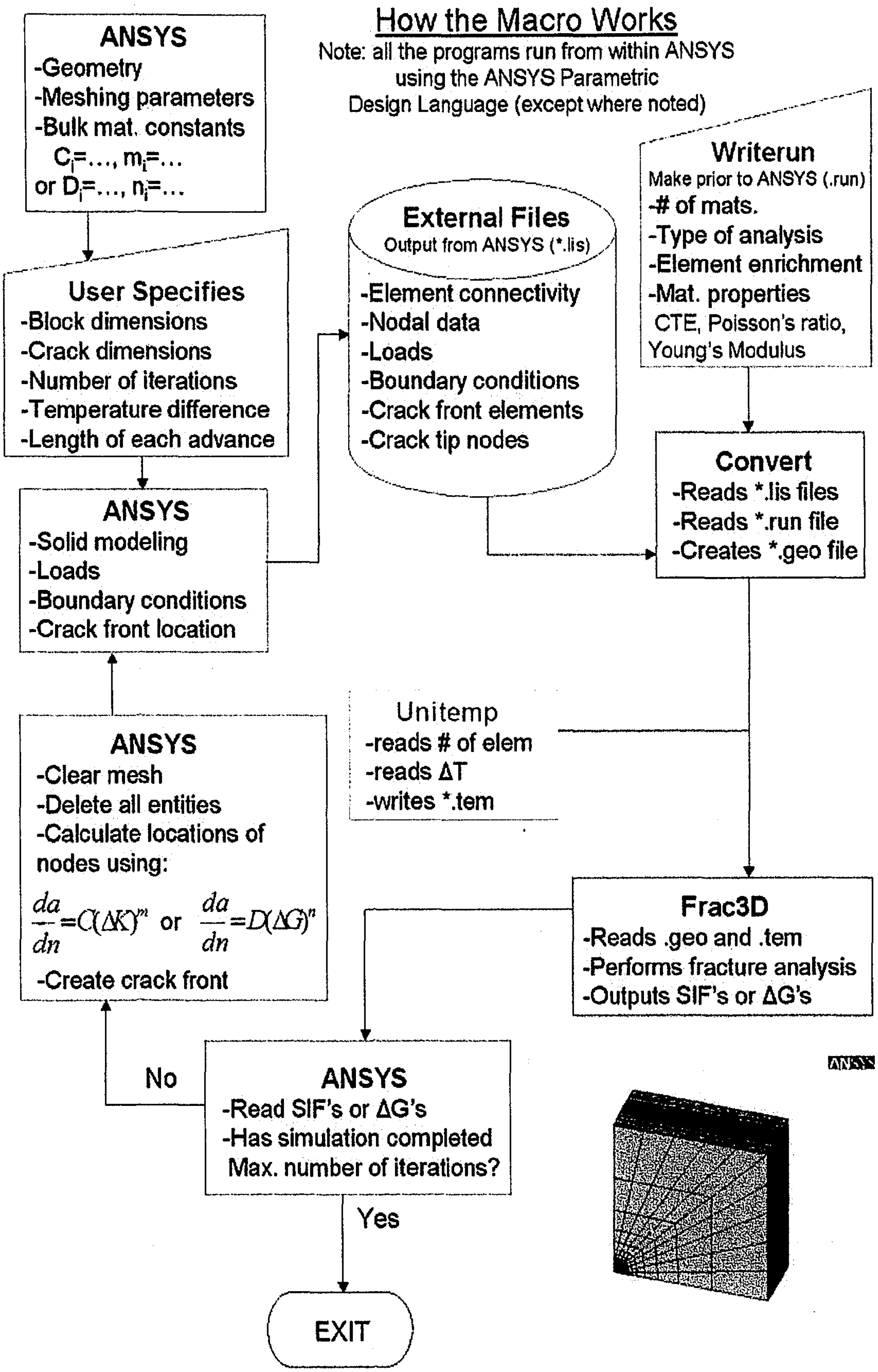

Figure 14: Flow chart describing the workings of the crack advance algorithm.

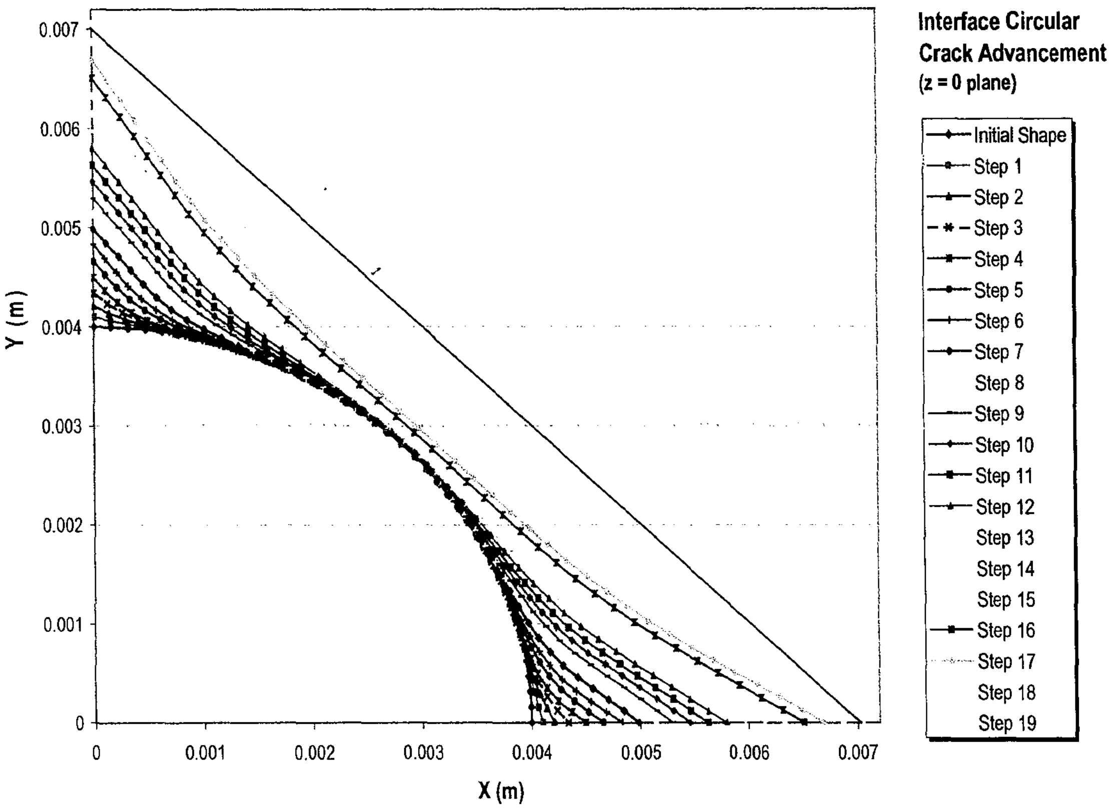

Figure 15: Plot of the nodal points of the advancing quarter-circular corner crack. The straight line is to illustrate the curvature of the crack front. Note: Figure 18 plots the number of cycles to reach each crack front (step 19 requires 4.0 x 10^4 cycles).

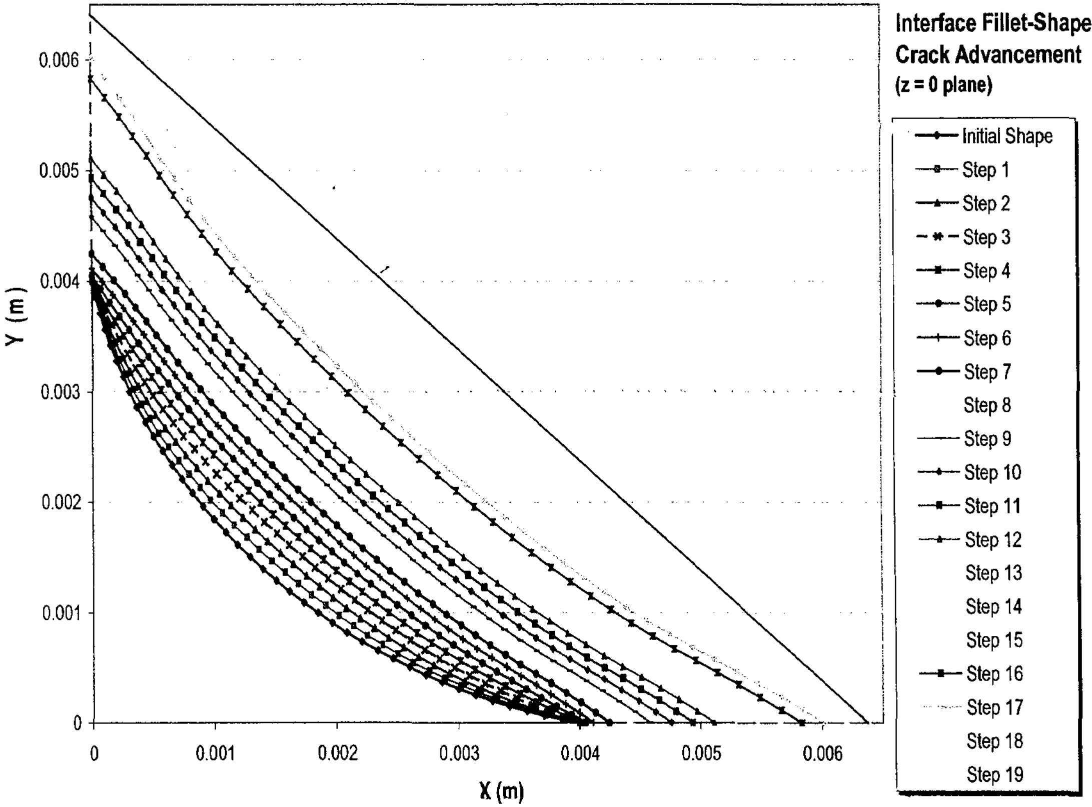

Figure 16: Plot of the nodal points of the advancing fillet-shaped crack front. The straight line is to illustrate the curvature of the crack front. Note: Figure 18 plots the number of cycles to reach each crack front (step 19 requires 7.1 x 10^4 cycles).

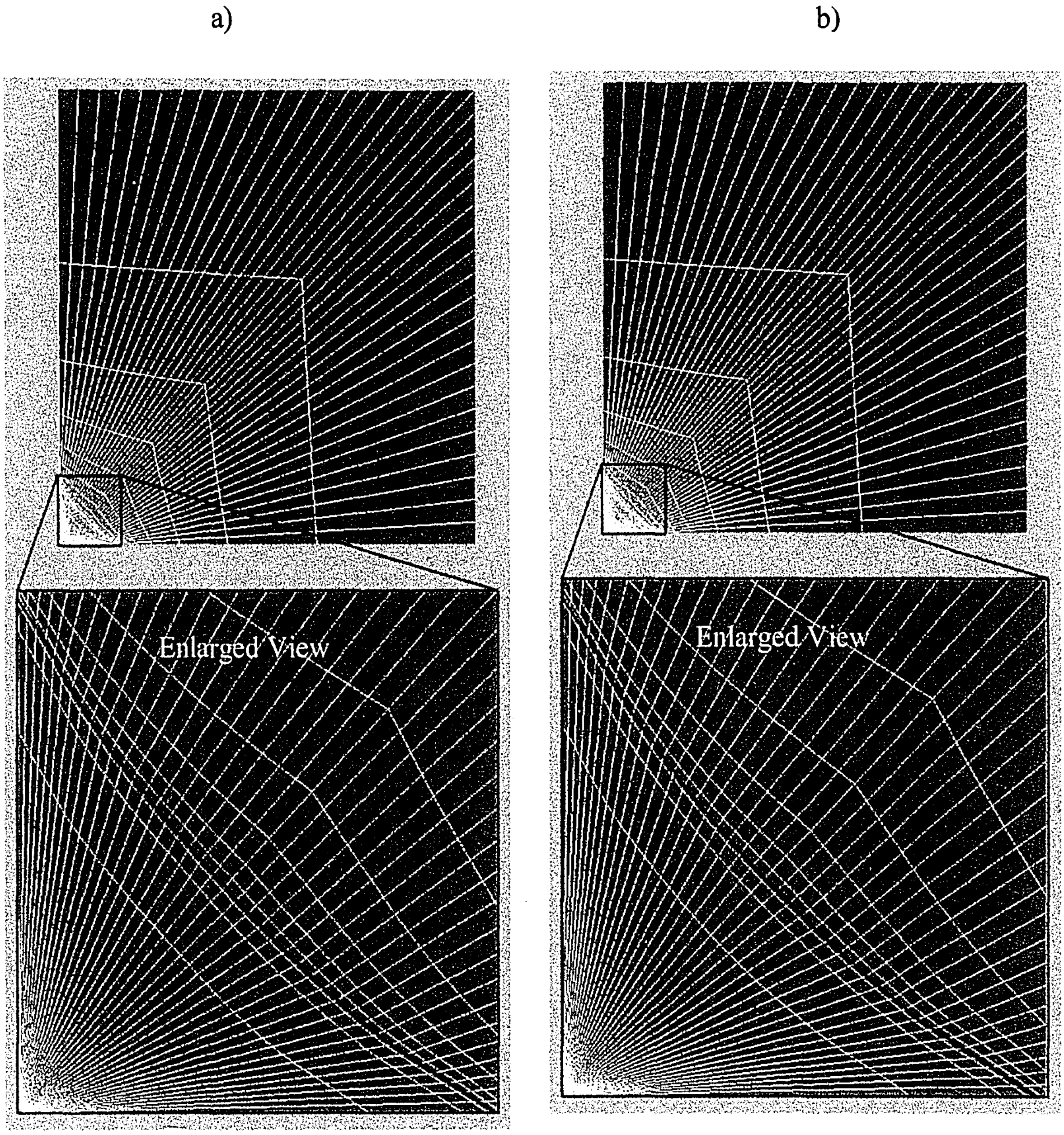

Figure 17: Finite element meshes after 20 steps. They are a) the circular crack and b) the fillet-shaped crack.

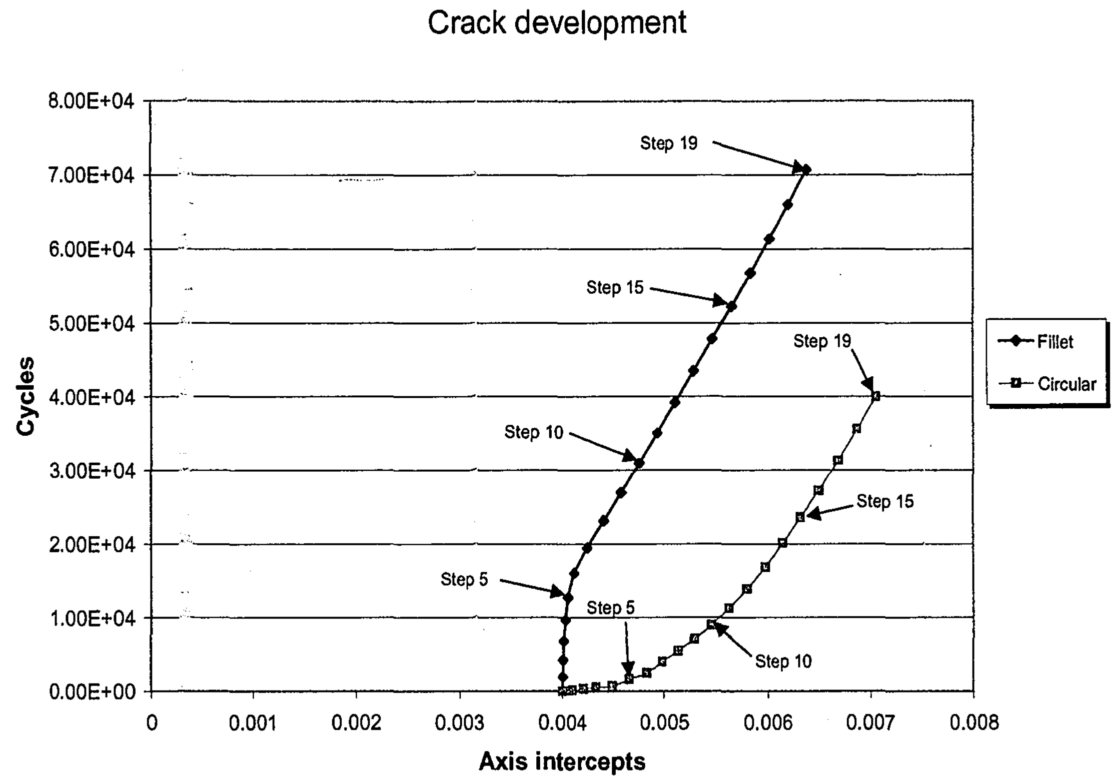

Figure 18: Plot of the location of the free surface node vs. the number of thermal cycles undergone to reach this location.

Note: Each data point represents one crack advance step.

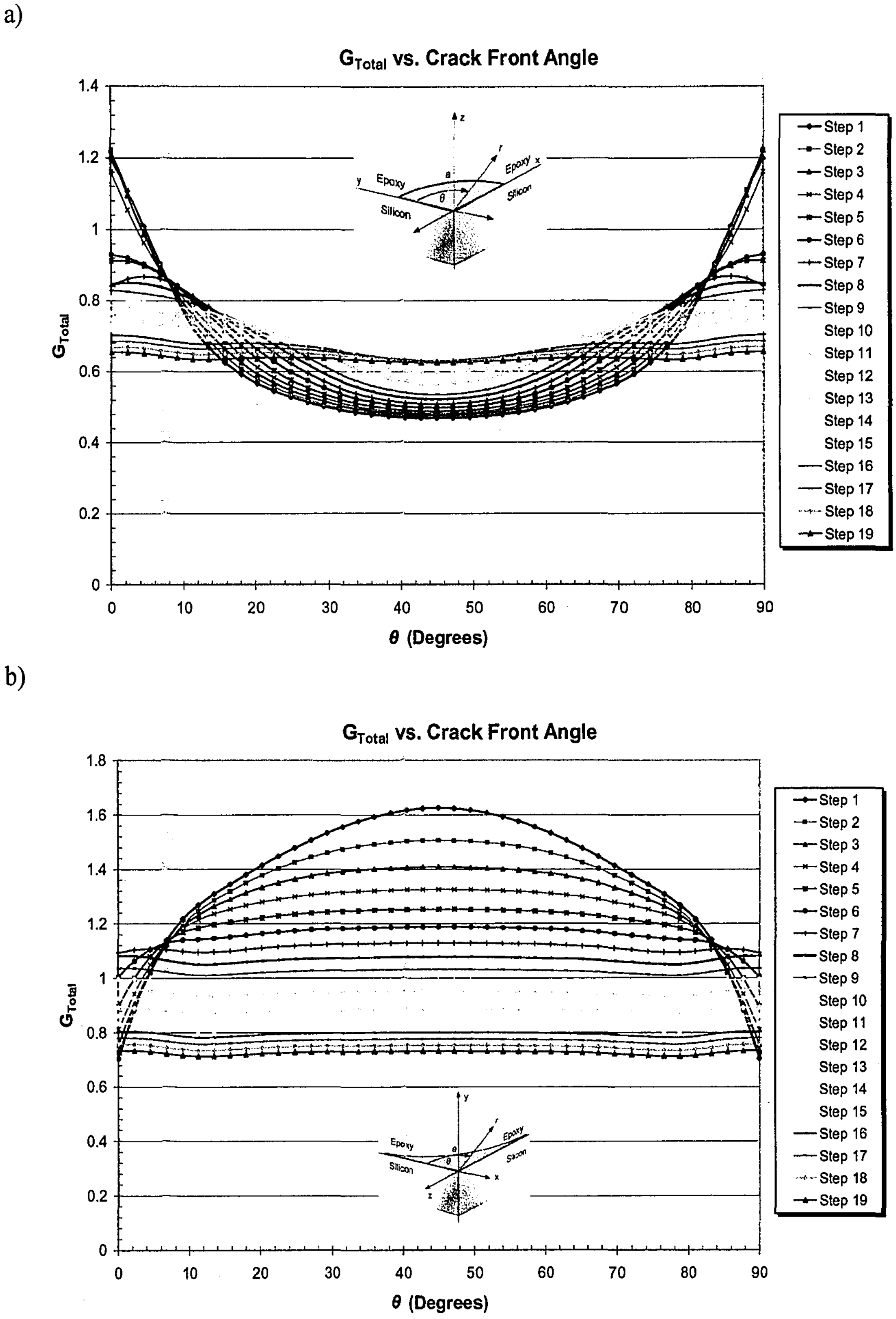

Figure 19: Plots of the total strain energy release rates over the entire propagation of the crack front for a) the quarter-circular case and b) the fillet-shaped crack.

Note: See Figure 9 for the normalization equations.

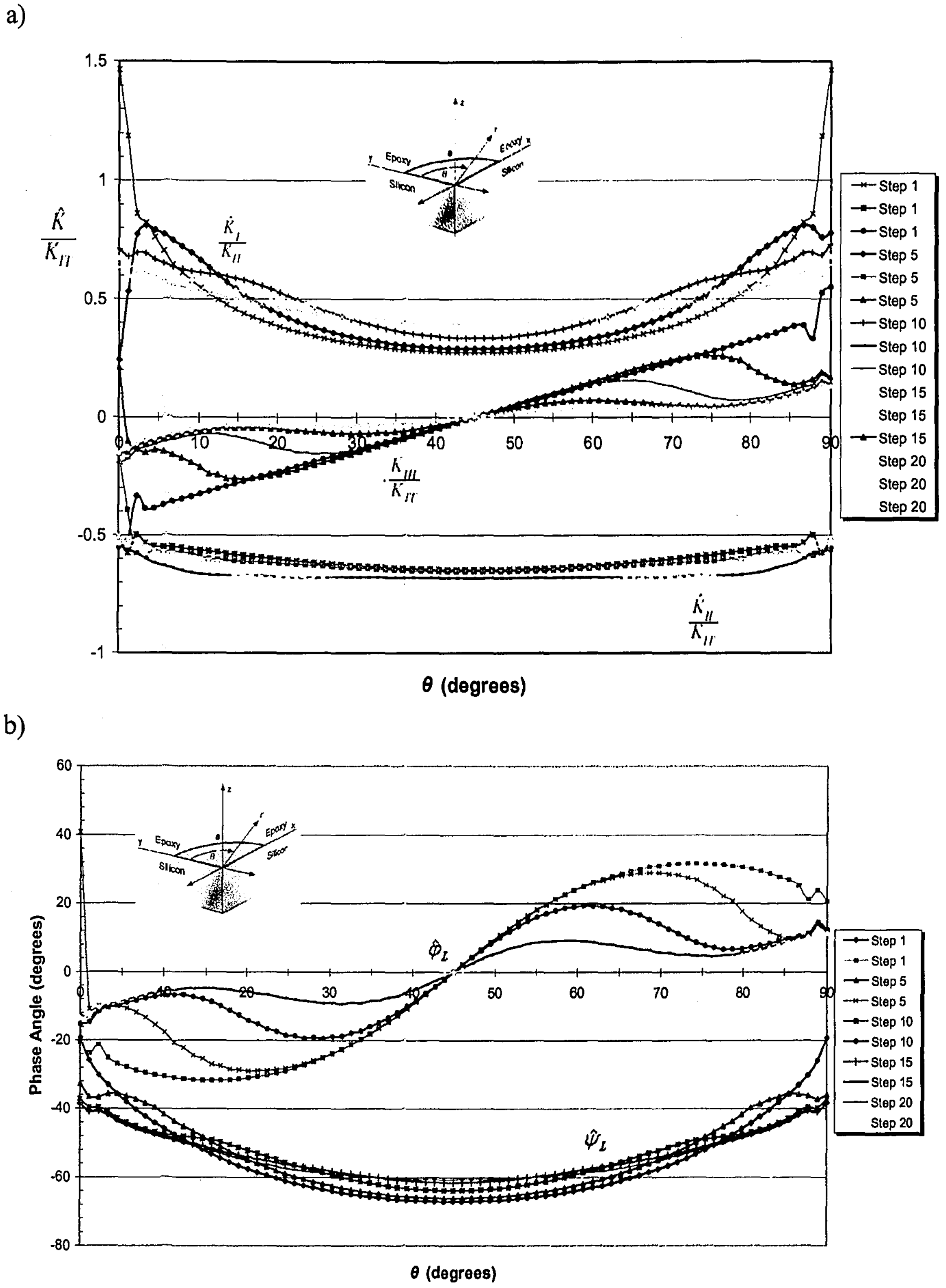

Figure 20: The development of a) the normalized stress intensity factors and b) the rotated phase angles over the course to the iterations in the quarter-circular corner crack. Results shown every five steps.

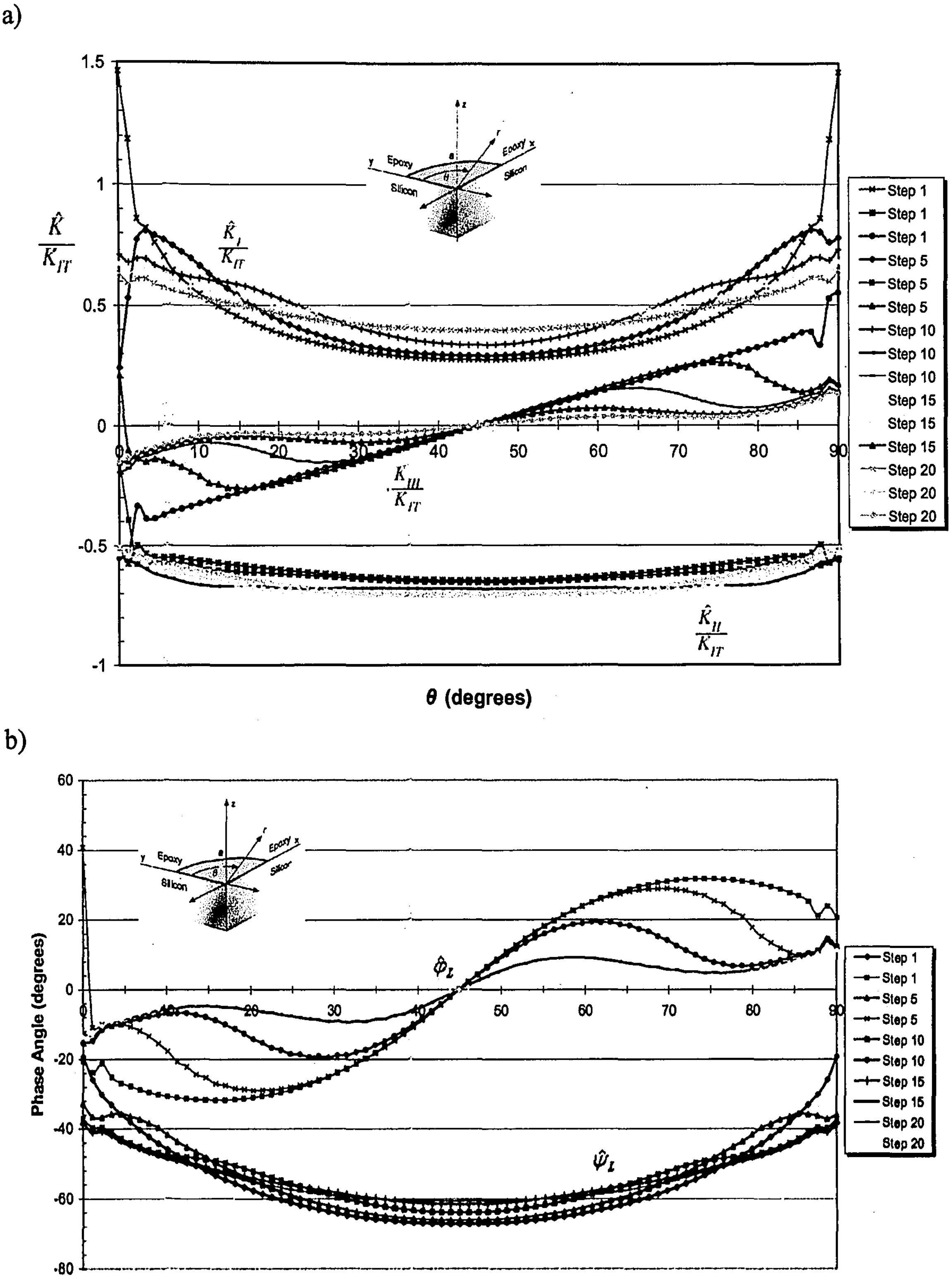

Figure 20: The development of a) the normalized stress intensity factors and b) the rotated phase angles over the course to the iterations in the quarter-circular corner crack. Results shown every five steps.

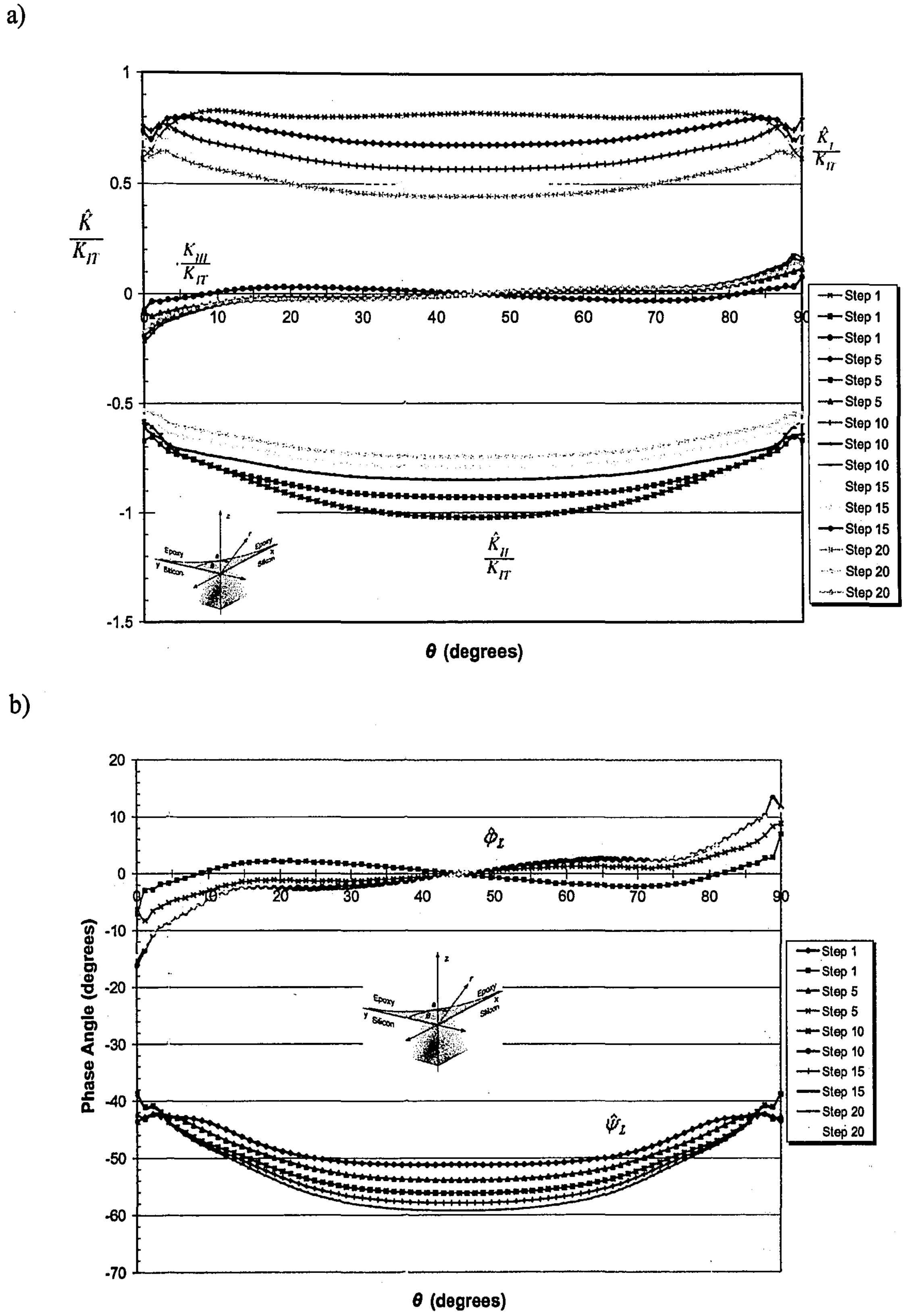

Figure 21: The development of a) the normalized stress intensity factors and b) the rotated phase angles over the course to the iterations in the fillet-shaped corner crack. Results shown every five steps.

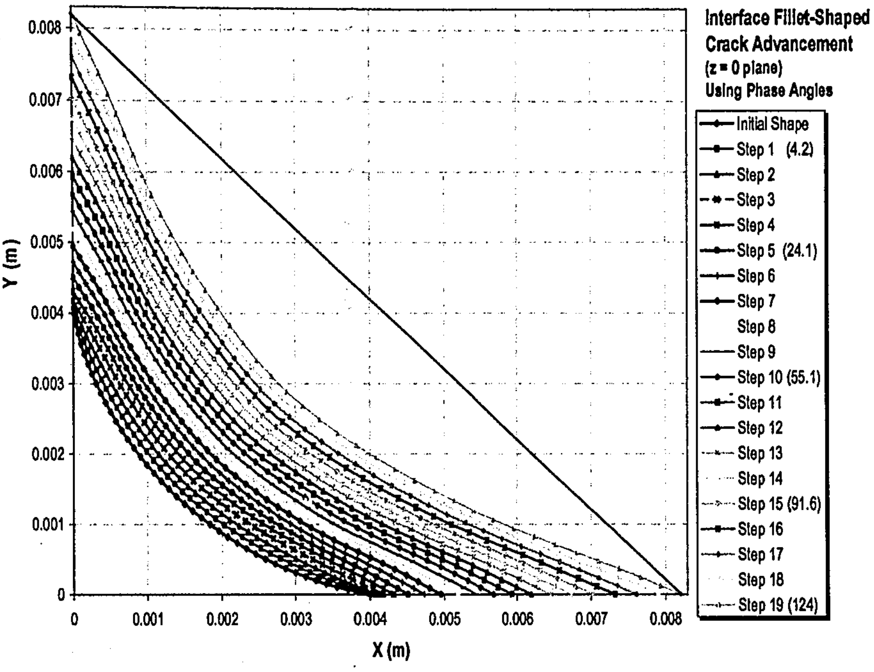

Figure 22: Plot of the nodal points of the advancing quarter-circular corner crack. The straight line is to illustrate the curvature of the crack front.

Note: The number of cycles to reach the current step is shown in parenthesis after every 5 steps (number of cycles in 100,000's).

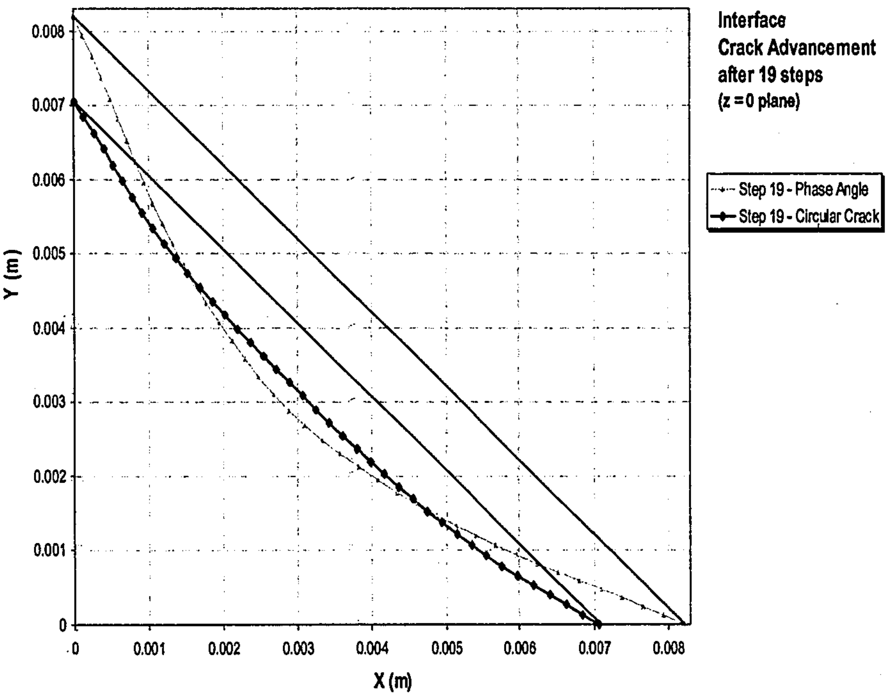

Figure 23: A comparison of the final step of the circular crack and the phase angle controlled crack.

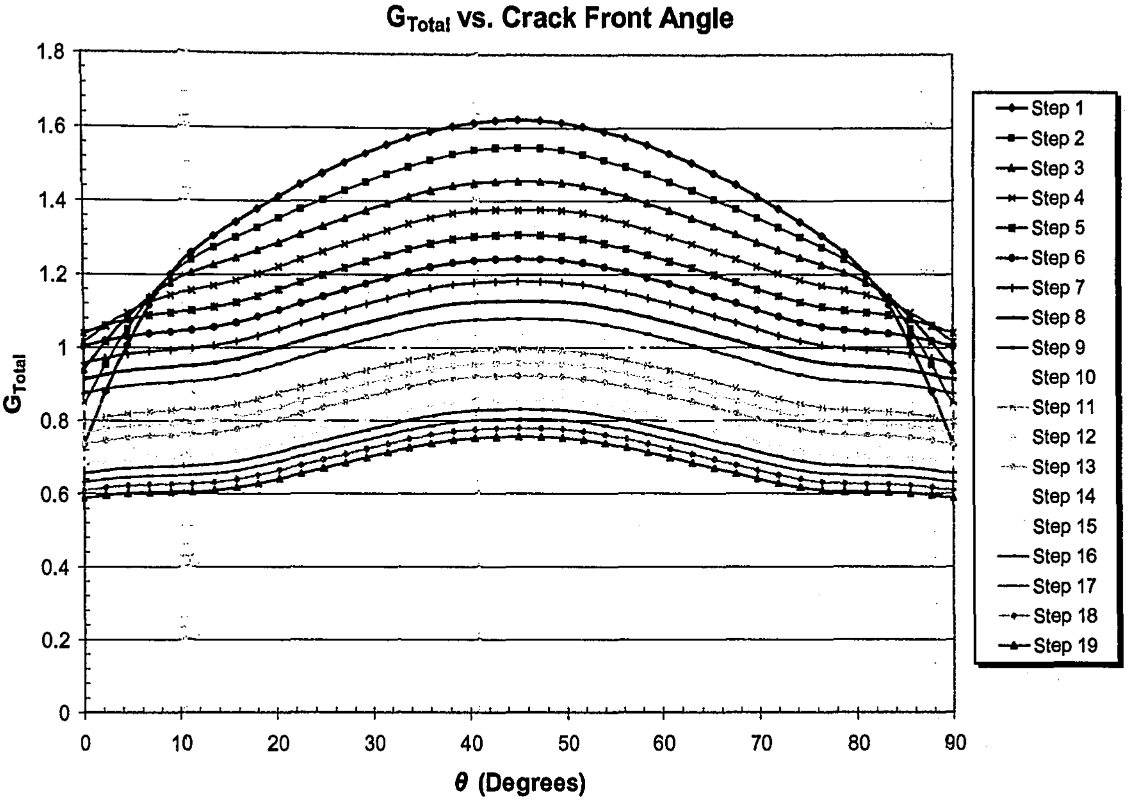

Figure 24: Plots of the total strain energy release rates over the entire propagation of the crack front for the fillet-shaped case using phase angles to control crack advances.

Note: See Figure 9 for the normalization equations.

References

[1] H.C. Cao and A.G. Evans, 'An Experimental Study of the Fracture Resistance of Bimaterial Interfaces', *Mechanics of Materials*, 7, 295 – 304 (1989).

[2] Jianjun Wang, Daqing Zou, Minfu Lu, Wei Ren, Sheng Liu, 'Evaluation of Interfacial Fracture Toughness of a flip-chip Package and a Bimaterial System by a Combined Experimental and Numerical Method', *Engineering Fracture Mechanics*, **64**, 781 – 797 (1999).

[3] H.F. Nied, 'Mechanics of Interface Fracture with Applications in Electronic Packaging', *Special Issue on Interface Reliability, IEEE Transactions on Devices and Materials Reliability*, accepted for publication.

[4] M.R. Begley and J.M. Ambrico, 'Delamination of Thin Films From Two-Dimensional Interface Flaws at Corners and Edges', *International Journal of Fracture*, **112**, 205 – 222 (2001), <http://www.people.virginia.edu/~mrb3h/papers/p5.pdf> (2003, December 3).

[5] X.B. Lin and R.A. Smith, 'Finite Element Modeling of Fatigue Crack Growth of Surface Cracked Plates, Part I: The Numerical Technique', *Engineering Fracture Mechanics*, **63**, 503 – 522 (1999).

[6] J.M. Snodgrass, D. Pantelidis, M.L. Jenkins, J.C. Bravman, R.H. Dauskardt, 'Subcritical Debonding of Polymer/Silica Interfaces Under Monotonic and Cyclic Loading', *Acta Materialia*, **50**, 2395 – 2411 (2002).

[7] J. W. Hutchinson and Z. Suo, "Mixed Mode Cracking in Layered Materials," *Advances in Applied Mechanics*, Vol. 29, Hutchinson, J. W., and Wu (eds), T. Y., 63–191, Academic Press, NY (1992).

[8] J.R. Rice, "Elastic Fracture Mechanics Concepts for Interfacial Cracks," *Journal of Applied Mechanics*, vol. 55, pp 98-103, (1988).

[9] X.B. Lin and R.A. Smith, 'An Improved Numerical Technique for Simulating the Growth of Planar Fatigue Cracks', *Fatigue & Fracture of Engineering Materials & Structures*, **20**, 1363 - 1373 (1997).

[10] X.B. Lin and R.A. Smith, 'Finite Element Modeling of Fatigue Crack Growth of Surface Cracked Plates, Part II: Crack Shape Change', *Engineering Fracture Mechanics*, **63**, 523 - 540 (1999).

[11] X.B. Lin and R.A. Smith, 'Finite Element Modeling of Fatigue Crack Growth of Surface Cracked Plates, Part III: Stress Intensity Factor and Fatigue Crack Growth Life', *Engineering Fracture Mechanics*, **63**, 541 - 556 (1999).

[12] P.E. O'Donoghue, S.N. Atluri, D.S. Pipkins, 'Computational Strategies for Fatigue Crack Growth in Three Dimensions with Application to Aircraft Components', *Engineering Fracture Mechanics*, **52**, 51-64 (1995).

[13] P. Krysl and T. Belytschko, 'The Element Free Galerkin Method for Dynamic Propagation of Arbitrary 3-D Cracks', *International Journal for Numerical Methods in Engineering*, **44**, 767-800 (1999).

[14] R. Galdos, 'A Finite Element Technique to Simulate the Stable Shape Evolution of Planar Cracks with an Application to a Semi-Elliptical Surface Crack in a Bimaterial Finite Solid', *International Journal for Numerical Methods in Engineering*, **40**, 905 – 917 (1997).

[15] T.J. Curtin, R.A. Adey, J.M.W. Baynham and P. Marais, 'Fatigue Crack Growth Simulation for Complex Three-Dimensional Geometry and Loading', n.d. <http://www.beasy.com/publications/plane/paper3.pdf> (2003, December 3).

[16] S. Mellings, J. Baynham, and R.A. Adey, 'Fully Automatic 3D Crack Growth with BEM,' http://www.beasy.com/images/pdf/publications/papers/bem_final.pdf

[17] S. Mellings, J. Baynham, R.A. Adey, and T. Curtin, 'Durability Prediction Using Automatic Crack Growth Simulation,' http://www.beasy.com/images/pdf/publications/DurabilityPrediction.pdf

[18] P. Hunter and A. Pullan, 'FEM/BEM Notes, Department of Engineering Science, The University of Auckland, New Zealand', n.d. <http://www.esc.auckland.ac.nz/Academic/Texts/fembemnotes.pdf> (2003, December 3).

[19] B.J. Carter, P.A. Wawrzynek and A.R. Ingraffea, 'Automated 3-D Crack Growth Simulation', *International Journal for Numerical Methods in Engineering*, **47**, 229 – 253 (2000).

[20] B.J. Carter, C.S. Chen, L.P. Chew, N. Chrisochoides, G.R. Gao, G. Heber, A.R. Ingraffea, R. Krause, C. Myers, D. Nave, K. Pingali, P. Stodghill, S. Vavasis and P.A. Wawrzynek, 'Parallel FEM Simulation of Crack Propagation - Challenges, Status, and Perspectives', n.d. <http://ipdps.eece.unm.edu/2000/irreg/18000444.pdf> (2003, February, 11).

[21] W.T. Riddel, A.R. Ingraffea, P.A. Wawrzynek, 'Experimental Observations and Numerical Predictions of Three-Dimensional Fatigue Crack Propagation', *Engineering Fracture Mechanics*, **58** (4), 293 – 310 (1997).

[22] Y.H. So, P. Garrou, J.H. Im, and D.M. Scheck, 'Benzocyclobutene-Based Polymers for Microelectronics', *Chemical Innovation*, Vol. 31, No. 12, 40 – 47 (2001) n.d. <http://pubs.acs.org/subscribe/journals/ci/31/i12/html/12so.html> (2003, December 3).

[23] A.O. Ayhan and H.F. Nied, 'Stress Intensity Factors for Three-Dimensional Surface Cracks Using Enriched Elements', *International Journal for Numerical Methods in Engineering*, **54**, 899 – 921 (2002).

[24] A.O. Ayhan and H.F. Nied, 'FRAC3D – Finite Element Based Software for 3-D and Generalized Plain Strain Fracture Analysis (Second Revision)', October, (1999).

[25] M. Heffes, 'ANSYS to FRAC3D Translator Guide', June, (2001).

[26] M. Heffes, 'FRAC3D TUTORIAL: Using ANSYS to Create a Mesh with a Circular Crack', June, (2001).

[27] M. Heffes, 'FRAC3D TUTORIAL: Using ANSYS to Create a Mesh with a Straight Crack', June, (2001).

Vita

Alexander Frantz Herr

Early Life: Born March 1, 1979 **Lancaster, PA**
First son of Daniel C. and Caroline D. Herr
Graduate of Lampeter-Strasburg High School, Lampeter, PA

Education: **Lehigh University** **Bethlehem, PA**
Masters of Science, Jan 2004.
Research in fracture mechanics and its applications to microchip packages.

Lafayette College **Easton, PA**
Bachelor of Science in Mechanical Engineering, May 2001
Bachelor of Arts in International Studies, May 2002
Marquis Scholar – Lafayette College's highest academic scholarship – four years
Lafayette College Dean's List
Studied abroad in Brussels in spring of 1999, three weeks in China in January 2000, and seven weeks in Spain during the summer of 2001

Experience: **Lehigh University** **Bethlehem, PA**
Teaching Assistant 9/01 – 5/03
During first four semesters, assisted with two lab courses. Both fall semesters one of the labs was a senior solid mechanics lab studying photoelasticity and shadow moiré which required sizable lab reports. The other lab is a sophomore lab in which students complete basic experiments and are introduced to data acquisition and transducers.
Spring semesters, assisted the manufacturing course. Involved instruction in manufacturing topics, aided in machining molds for injection molding, and culminated in arranging and overseeing the end of the semester race.

Ove Arup & Partners **Detroit, MI**
Internship 5/00 - 8/00
Assisted consulting firm with computer-aided engineering in the automotive industry. Learned the basics of finite element analysis, including meshing to predetermined specifications (using Hypermesh), writing decks for static (Nastran) and non-linear (LS-Dyna) code, and post-processing. Also learned about the workings of an engineering CAE firm and tasks that consulting engineers perform. Worked on-site with a client and interacted directly with designers.

Memberships and Accolades:
Tau Beta Pi member – mechanical engineering honor fraternity

END OF
TITLE